

A new galaxy spectral energy distribution model consistent with the evolution of dust

Kazuki Y. Nishida,¹* Tsutomu T. Takeuchi,^{1,2} Takuma Nagata,¹ and Ryosuke S. Asano¹

¹*Division of Particle and Astrophysical Science, Nagoya University, Furo-cho, Chikusa-ku, Nagoya, 464–8602, Japan*

²*The Research Center for Statistical Machine Learning, The Institute of Statistical Mathematics, 10-3 Midori-cho, Tachikawa, Tokyo 190–8562, Japan*

Accepted XXX. Received YYY; in original form ZZZ

ABSTRACT

The spectral energy distribution (SED) of galaxies provides fundamental information on the related physical processes. However, the SED is significantly affected by dust in its interstellar medium. Dust is mainly produced by asymptotic giant branch stars and Type II supernovae. In addition, the dust mass increases through the metal accretion, and the grain size changes by the collisions between the grains. The contribution of each process and the extinction depend on the size distribution. Therefore, the SED model should treat the evolution of the dust mass and size distribution. In spite of the importance of dust evolution, many previous SED models have not considered the evolution of the total mass and size distribution in a physically consistent manner. In this work, we constructed a new radiative transfer SED model, based on our dust evolution model consistent with the chemical evolution. To reduce the computational cost, we adopted the mega-grain and the one-dimensional plane parallel galaxy approximation. As a fiducial case, we calculated Milky Way-like galaxy SEDs at various ages under the closed-box model. We found that a galaxy at the age of 100 Myr does not produce small grains such as polycyclic aromatic hydrocarbons. After 1 Gyr, we observed a drastic increase of infrared emission and attenuation caused by a rapid increase of dust mass. This phenomenon can be treated appropriately for the first time by our new model. This model can be used for the SED fitting to a galaxy at any stage of evolution.

Key words: dust, extinction – galaxies: evolution – ISM: evolution – radiative transfer – galaxies: ISM – galaxies: disc

1 INTRODUCTION

The spectral energy distribution (SED) fitting is a fundamental method to extract the information of the physical processes in galaxies (e.g., star formation rate: SFR, stellar mass, dust mass) from observational data. Stars emit photons with wavelengths ranging from ultraviolet (UV) to near-infrared (NIR). Dust grains absorb and scatter the photons emitted from stars, and re-emit the absorbed energy at mid-infrared (MIR) to far-infrared (FIR). In addition to the radiative aspect of a galaxy, dust grains promote the formation of hydrogen molecules on the surface of the grains (e.g., Hollenbach & McKee 1979; Hirashita & Ferrara 2002; Cazaux et al. 2005). Since hydrogen molecules are one of the fundamental ingredients of the star formation, dust grains directly activate the star formation in galaxies.

Dust is a solid grain consisting of the elements heavier than helium, and is produced by stellar mass loss and supernovae (SNe). Outflows from low- and intermediate-mass stars during the thermally pulsing asymptotic giants branch (TP-AGB) phase and Type II SNe (SNe II) are considered to be the primary sources of dust (e.g., Nozawa et al. 2007; Bianchi & Schneider 2007; Zhukovska et al. 2008). Dust grains are formed by condensation of heavy elements in the atmosphere of massive stars, and only the grains that could survive the reverse shock of the SN are finally expelled into the interstellar medium (ISM). Then, the blast waves from SNe propagating in the

ISM also destroy dust grains (e.g., Jones et al. 1994, 1996; Nozawa et al. 2003, 2006; Zhukovska et al. 2008; Yamasawa et al. 2011). This destruction process has been confirmed by observations of several supernova remnants (e.g., Borkowski et al. 2006; Arendt et al. 2010). Details of the dust grain survival still remain controversial. It might depend on their composition and size¹ (e.g., Nozawa et al. 2007; Gall et al. 2014; Slavin et al. 2020), and others claim that it depends on the clumpiness of the ejecta (e.g., Biscaro & Cherchneff 2016). In addition, Matsuura et al. (2019) argue that the dust destruction by the SN are suppressed because the atoms can stick to the surviving dust grain in the passage of the forward shock region and it can reform or increase dust grains. Observations of SN remnants (SNRs) do not give a final answer, since dust mass and composition are significantly different among observed SNRs.

In addition to the dust production from stars, dust growth in the ISM is also an important process, and necessary to explain the large amount of dust present in galaxies (e.g., Asano et al. 2013a; Zhukovska 2014; Michałowski 2015; Lesniewska & Michałowski 2019). In the cold phase of ISM, metal is accreted onto the dust grain surface to increased the size and total mass of the dust (e.g., Dwek 1998; Zhukovska et al. 2008; Michałowski et al. 2010; Hirashita &

¹ Terminologies such as grain size, size distribution, etc. are often used in articles related to dust. Throughout this paper, when we mention “size” of dust grain, it always mean the dust grain radius under the assumption of spherical shape.

* E-mail: nishida.kazuki@nagoya-u.jp

Kuo 2011; Asano et al. 2013a). The size distribution of the dust is also changed through the collisions between dust grains (e.g., Yan et al. 2004; Jones et al. 1996; Hirashita & Yan 2009; Kuo & Hirashita 2012).

Which process controls the mass of dust varies greatly, depending on the age and the environment of the galaxy, and it is still actively debated from several different points of view. The SNe II dominates the dust production, especially in very young galaxies, because SNe II have a shorter lifetime (< 30 Myr) than AGB stars (> 150 Myr) (e.g., Morgan & Edmunds 2003; Marchenko 2006; Dwek et al. 2007; Valiante et al. 2009; Gall et al. 2011a,b; Liu & Hirashita 2019; De Looze et al. 2020; Burgarella et al. 2020; Nanni et al. 2020). We should note, however, that the contribution of AGB cannot be ignored even in galaxies with the age of 500 Myr, when the star formation rate (SFR) is high (Valiante et al. 2009).

The debate of dust grain growth in high- z galaxies has not been settled. In high- z galaxies, several studies claim that the process is not effective because there is not enough time to growth, low gas density, and high temperature (e.g., Ferrara et al. 2016; Ceccarelli et al. 2018). Since dust growth in the ISM is strongly affected by the metallicity in a galaxy (e.g., Inoue 2003; Asano et al. 2013a), they claim that it might not be very important in young galaxies with low metallicity. However, other studies have shown that the dust mass in distant galaxies cannot be explained without considering metal accretion (e.g., Pipino et al. 2011; Valiante et al. 2011; Zhukovska 2014; Michałowski 2015; Mancini et al. 2015; Lesniewska & Michałowski 2019; Rouillé et al. 2020).

Asano et al. (2013a) defined the critical metallicity, Z_{cr} , as the metallicity of the ISM, at which the production rate of dust from stars (AGB and SNe II) become equal to the mass growth rate in the ISM. When the metallicity reaches Z_{cr} , the dust mass increases suddenly and nonlinearly. This rapid increase in dust mass is caused by the following process (e.g., Hirashita & Yan 2009; Asano et al. 2013a,b). First, the metal accretion depends on the metallicity and total surface area of the dust grains. As the dust size increases through the metal accretion, yet another process of dust evolution in the ISM, shattering, is more likely to occur. This process is basically the collision of grains with each other and redistribute the mass of dust into smaller-sized grains. When the shattering becomes effective, the total surface area of the dust grain per mass increases, and the metal accretion becomes more efficient. This cycle leads to the sharp increase of the total dust mass along with metallicity. Therefore, not only the total dust mass, but also it is of vital importance to take into account the grain size distribution to discuss the evolution of dust in galaxies.

The absorption and scattering coefficients of dust as a function of wavelength depend on the size and composition of grains. When a dust grain absorbs light, its temperature rises and the absorbed energy is re-emitted at longer wavelengths (mainly IR). The wavelength of the re-emission depends on the instantaneous temperature of the grain, and the temperature strongly depends on the size of the grain. Thus, as already mentioned, the mass, size, and composition of dust grains play a fundamental role in shaping the SED of a galaxy. Fitting to the SED of distant galaxies by an empirical dust emission model without evolution may lead to erroneous results. This happens, for example, when we use a model in which the dust size distribution is constant. Recently, some galaxies with a large amount of dust ($M_{\text{dust}} > 10^6 M_{\odot}$) have been observed at $z > 6$ (e.g., Watson et al. 2015; Laporte et al. 2017; Tamura et al. 2019). Now it is a proper moment to develop a new SED model based on the theory of dust evolution, after the advent of the Atacama Large

Millimeter/Submillimeter Array (ALMA) and other large facilities at this wavelength range.

The dust evolution in the ISM has been considered by a number of previous studies (e.g., Dwek 1998; Calura et al. 2008; da Cunha et al. 2010; Asano et al. 2013a,b, 2014; Mancini et al. 2015; Schneider et al. 2016; Ginolfi et al. 2018; De Vis et al. 2017, 2019; Hirashita & Aoyama 2019; De Looze et al. 2020; Nanni et al. 2020; Burgarella et al. 2020). We put our basis on the theoretical framework of dust evolution proposed by Asano et al. (2013a,b, 2014) and Nozawa et al. (2015) (hereafter Asano model) to develop a new radiative transfer SED model. The Asano model considers SNe II and AGB stars as dust production sources, and not only the metal accretion but also shattering and coagulation as the dust evolution process in the ISM, which enables us to determine the dust mass and size distribution in all galaxy ages from a first principle. Hirashita & Aoyama (2019) developed a dust evolution model also based on the Asano model, but with a better computational performance to apply to cosmological simulations. Recall that the Asano model considers different physical quantities (e.g., ambient gas density of SN, hydrogen gas density, and magnetic field strength) for various galaxies to treat the dust destruction by SN and dust collisions. However, considering dust on the cosmological scale, it is impossible to reach a galaxy scale resolution. Therefore, Hirashita & Aoyama (2019) adopt many simplifications to optimize their model for the simulations. In contrast, since we aim at calculating SED of an individual galaxy, we make a maximal use of the Asano model.

There have been several SED models that include the evolution of dust in the ISM. For example, Schurer et al. (2009) is the SED model which is based on the dust model of Calura et al. (2008). They calculate the chemical evolution in a single gas phase and dust evolution including metal accretion. However, since Schurer et al. (2009) do not consider shattering and coagulation, the rapid increase of the total dust mass does not occur. Version 3 of PÉGASE (Fioc & Rocca-Volmerange 2019) considers the evolution of dust mass, and can calculate not only the radiation from stars but also the extinction by dust grain and the radiation of dust with a stochastic temperature distribution. PÉGASE does not take into account the dust size distribution, and assumes that the fraction and the size distribution of each grain species do not evolve. In this paper, we construct a new galaxy SED model, including the dust evolution theory proposed by Asano et al. (2013a,b, 2014). We adopt the mega-grain approximation (MGA) with a one-dimensional plain parallel galaxy (Varosi & Dwek 1999; Inoue 2005) to make the radiative transfer calculation faster.

This paper is organized as follows. In Section 2, we introduce how to calculate the SED for each component. In Section 3, as an example of our SED model, we show the SED of a Milky Way (MW)-like galaxy. In Section 4, we discuss the effect of parameters on the model SEDs. Section 5 is devoted to the conclusions.

2 METHODS: CONSTRUCTION OF SED MODEL

To construct a galaxy SED model, we synthesis the stellar SED calculated by version 2 of PÉGASE (Fioc & Rocca-Volmerange 1999, PÉGASE.2), the dust evolution model based on Asano et al. (2013a,b, 2014), dust attenuation calculated by radiative transfer with MGA in a one-dimensional galaxy (Varosi & Dwek 1999; Inoue 2005), and the dust emission by a Monte Carlo simulation. In this section, we present how to calculate each component. §2.1 introduces the equation of mass evolution in a galaxy. §2.2 shows the details of the dust chemical evolution model. §2.3 is the overview of calculation

of stellar SED by PÉGASE.2. §2.4 and 2.5 show dust properties with mega-grain approximation and radiative transfer in one-dimensional galaxy, respectively. In §2.6 and 2.7, we explain the calculation of the dust temperature distribution by Monte Carlo simulation and the dust emission by the distribution.

2.1 Equations governing galaxy evolution

We consider stars, gases and dust grains as the components of a model galaxy. For simplicity, we assume a one-zone galaxy model, where physical quantities vary uniformly over the entire galaxy. The time evolution of the total stellar mass $M_*(t)$, the ISM mass $M_{\text{ISM}}(t)$, the metal mass $M_Z(t)$, and the dust mass $M_d(t)$ at an age of galaxy t are represented as (Lisenfeld & Ferrara 1998; Asano et al. 2013a),

$$\frac{dM_*(t)}{dt} = \text{SFR}(t) - R(t), \quad (1)$$

$$\frac{dM_{\text{ISM}}(t)}{dt} = -\text{SFR}(t) + R(t) + \frac{dM_{\text{infall}}(t)}{dt}, \quad (2)$$

$$\frac{dM_Z(t)}{dt} = -Z(t)\text{SFR}(t) + R_Z(t) + Y_Z(t), \quad (3)$$

$$\frac{dM_d(t)}{dt} = -D(t)\text{SFR}(t) + Y_d(t) - \left(\frac{dM_d(t)}{dt}\right)_{\text{SN}} + \left(\frac{dM_d(t)}{dt}\right)_{\text{acc}}, \quad (4)$$

where $\text{SFR}(t)$ is the star formation rate, and $R(t)$ and $R_Z(t)$ are the mass of the gas and metal taken into stars from ISM and returned to ISM when stars die per unit time, respectively. dM_{infall}/dt is the infall gas rate, which is assumed to be zero in this paper except §4.5. $Z(t) \equiv M_Z/M_{\text{ISM}}$ is the metallicity, and $D(t) \equiv M_d/M_{\text{ISM}}$ is the mass fraction of dust with respect to the total amount of metal. $Y_Z(t)$ and $Y_d(t)$ are the metal and dust masses newly produced by stars per unit time, respectively. $(dM_d(t)/dt)_{\text{SN}}$ and $(dM_d(t)/dt)_{\text{acc}}$ is the change of grain mass caused by SN shock and metal accretion. In the Asano model, three phases are supposed in the ISM: warm neutral medium (WNM, with gas temperature $T_{\text{gas}} = 6000$ K, and hydrogen number density $n_{\text{H}} = 0.3 \text{ cm}^{-3}$), cold neutral medium (CNM, with $T_{\text{gas}} = 100$ K, $n_{\text{H}} = 30 \text{ cm}^{-3}$), and molecular cloud (MC, with $T_{\text{gas}} = 25$ K, $n_{\text{H}} = 300 \text{ cm}^{-3}$) (Nozawa et al. 2015). In the MC, dust grains form icy mantle on the grain surface. (e.g., Kalvans 2017; Ceccarelli et al. 2018). However, since the properties of the icy mantle are not well understood yet, we do not consider its effect in this work. As for the dust growth in the ISM, metal accretion occurs only in CNM and MC, and shattering and coagulation occur in all three phases. Because metal accretion occurs effectively in high density regions, the grain growth in the MC is more prominent. In this paper, we fix the phase fraction of WNM, CNM, and MC to $\eta_{\text{WNM}} = 0.5$, $\eta_{\text{CNM}} = 0.3$, and $\eta_{\text{MC}} = 0.2$, respectively, the same values to that of Nozawa et al. (2015) used to reproduce the MW extinction curve. These fractions are constant throughout the calculation of the dust model. For each time step, the dust grain is redistributed into each ISM phase so that the mass fraction of each ISM phase is maintained. Thus, we consider the dust grain cycling between the different ISM phases. Also, we do not consider the outflow effects in this model. We assume that at the age of $t = 0$, the galaxy contains no stars and dust, and contains only zero-metallicity gas (i.e., $M_{\text{star}}(0) = M_Z(0) = M_d(0) = 0$, and $M_{\text{ISM}}(0)$ is total galaxy mass).

We adopt the Schmidt law (Schmidt 1959), $\text{SFR}(t) \propto M_{\text{ISM}}^n$ for SFR with $n = 1$ for simplicity, as

$$\text{SFR}(t) = \frac{M_{\text{ISM}}(t)}{\tau_{\text{SF}}}, \quad (5)$$

where τ_{SF} is the timescale of star formation. In this paper, initial galaxy mass $M_{\text{ISM}}(0)$ and τ_{SF} are set to be $10^{11} M_{\odot}$ and 3 Gyr as fiducial values. $R(t)$, $R_Z(t)$, and $Y_d(t)$ are represented as

$$R(t) = \int_{m_{\text{min}}(t)}^{100 M_{\odot}} [m - \omega(m, Z(t - \tau_m))] \phi(m) \times \text{SFR}(t - \tau_m) dm, \quad (6)$$

$$R_Z(t) = \int_{m_{\text{min}}(t)}^{100 M_{\odot}} [m - \omega(m, Z(t - \tau_m))] \phi(m) \times \text{SFR}(t - \tau_m) Z(t - \tau_m) dm, \quad (7)$$

$$Y_Z(t) = \int_{m_{\text{min}}(t)}^{100 M_{\odot}} m_Z(m, Z(t - \tau_m)) \phi(m) \text{SFR}(t - \tau_m) dm, \quad (8)$$

$$Y_d(t) = \int_{m_{\text{min}}(t)}^{100 M_{\odot}} m_d(m, Z(t - \tau_m)) \phi(m) \text{SFR}(t - \tau_m) dm, \quad (9)$$

where $m_{\text{min}}(t)$ is the lower limit mass of star which can explode at time t , $\phi(t)$ is the initial mass function (IMF), $\omega(m, Z(t - \tau_m))$, $m_Z(m, Z(t - \tau_m))$, and $m_d(m, Z(t - \tau_m))$ are the remnant mass which remains after a star explodes, and the metal mass and the dust mass newly produced by a star of mass m and metallicity $Z(t - \tau_m)$. As for ω and m_Z , we adopt Ventura et al. (2013) for AGB stars with mass $m = 1-8 M_{\odot}$ and metallicity $Z = (0.015, 0.4) Z_{\odot}$, and Kobayashi et al. (2006) for SNe II with progenitor mass $m = 13-40 M_{\odot}$ and metallicity $Z = (0.0, 0.05, 0.3, 1.0) Z_{\odot}$. We interpolate and extrapolate all data tables over mass and metallicity in this paper. τ_m is the lifetime of a star with mass m and we use the following equation by Raiteri et al. (1996),

$$\log \tau_m = a_0(Z) + a_1(Z) \log m + a_2(Z) (\log m)^2, \quad (10)$$

with

$$a_0(Z) = 10.13 + 0.07547 \log Z - 0.008084 (\log Z)^2, \quad (11)$$

$$a_1(Z) = -4.424 - 0.7939 \log Z - 0.1187 (\log Z)^2, \quad (12)$$

$$a_2(Z) = 1.262 + 0.3385 \log Z + 0.05417 (\log Z)^2. \quad (13)$$

This equation was obtained by fitting the calculation result of stars with stellar mass range $0.6-120 M_{\odot}$ and metallicity range $0.0004-0.05$ by the Padova group (Alongi et al. 1993; Bressan et al. 1993; Bertelli et al. 1994). We use the Salpeter IMF (Salpeter 1955):

$$\phi(m) \propto m^{-2.35}. \quad (14)$$

The IMF is normalized as

$$\int_{0.1 M_{\odot}}^{100 M_{\odot}} \phi(m) m dm = 1 M_{\odot}. \quad (15)$$

2.2 Dust evolution model

In this paper, we adopt the Asano model. The Asano model takes into account ten species for dust; C, Si, SiO_2 , Fe, FeS, Al_2O_3 , MgO, MgSiO_3 , Mg_2SiO_4 , and Fe_3O_4 (Nozawa et al. 2007; Zhukovska et al. 2008). Since the Asano model calculates the evolution for each dust species, the dust composition evolves with time. For simplicity in this work, we divide dust grains into two representative families, silicate and carbonaceous grains, for the grain growth and grain-grain collision, because the optical properties of other dust species are not well understood yet. Further, among the carbonaceous grains, the smaller ones are treated as polycyclic aromatic hydrocarbon (PAH) grains. The fraction of graphite in carbonaceous dust grain is obtained

by the following formula (Draine & Li 2007),

$$f_{\text{gra}} = \begin{cases} 0.01 & (a < 50 \text{ \AA}) \\ 0.01 + 0.99 \left[1 - \left(\frac{50 \text{ \AA}}{a} \right)^3 \right] & (a > 50 \text{ \AA}) \end{cases}. \quad (16)$$

Where a is the dust grain radius and the fraction of PAHs is defined as $f_{\text{PAH}} = 1 - f_{\text{gra}}$. Since the PAHs are divided into ionized and neutral PAHs, which have different optical properties. The fraction of ionized PAH is shown in Figure 7 of Li & Draine (2001). A part of carbonaceous grains could consist of amorphous carbon. According to Nozawa et al. (2015), graphite is accepted for reproducing the attenuation curve of nearby galaxy like MW, and amorphous carbon is accepted for galaxies that do not have 2175 Å bumps in the attenuation curve, such as high- z quasars. Since the differences between these compositions are not well understood yet, we only consider graphite grains in this work. It is also possible to take into account amorphous carbon in our SED model.

This model considers only AGB and SNe II as the sources of dust grains. For simplicity, we do not consider SNe Ia contributions because they are considered to be a very minor contributor to the total mass of dust (e.g., Calura et al. 2008).

The dust size distribution is represented by the dust number $f_X(a, t)$ and mass $\rho_X(m_d, t)$ distribution. $f_X(a, t) da$ and $\rho_X(m_d, t) dm_d$ are the number and mass density of dust grains with radii $[a, a + da]$ and mass $[m_d, m_d + dm_d]$ at time t , respectively. Where 'X' represents the dust species (C: carbonaceous or Si: silicate grain), a is the dust radius, and m_d is the dust grain mass. We assume that the dust grain has a constant density s and is spherical grain, so dust grain mass is

$$m_d = \frac{4}{3} \pi a^3 s. \quad (17)$$

The relation of dust number and mass density is expressed as

$$\rho_X(m_d, t) dm_d = m_d f_X(a, t) da. \quad (18)$$

In the initial condition of the galaxy, the dust mass of all sizes is set to be zero. Therefore, in the first time step of the computation, only the dust grain is produced by the stars. In the next time step, the dust size distribution produced by the stars evolves through the dust evolution process in the ISM. In the following, we explain the details of the Asano model.

2.2.1 Dust production by AGB

AGB stars are the final phase of the evolution of low and intermediate mass stars ($< 8 M_\odot$). They have the carbon-oxygen core and are burning hydrogen and helium surrounding the core. They release heavier elements in the ISM, and dust grains are formed in the ejecta. The dust size distribution produced by AGB stars depends on the progenitor mass and suggested that it is represented by a log-normal distribution with a peak at $\sim 0.1 \mu\text{m}$ by Winters et al. (1997). Further, Yasuda & Kozasa (2012) calculates dust formation by AGB stars with the hydrodynamical simulation including SiC production. They suggest that the mass distribution per unit logarithmic bin $a^4 f(a)$ is described by a log-normal distribution with a peak at 0.2–0.3 μm . We assume the size distribution of dust grains from AGB stars is represented by the log-normal with a peak at 0.1 μm with a standard deviation of $\sigma = 0.47$. This shape reproduces Figure 7 of Yasuda & Kozasa (2012). We assume the same size distributions for all dust species.

As for the dust mass produced by AGB stars, we adopt Ventura

et al. (2012, 2013). They consider AGB stars with a mass range of 1–8 M_\odot and metallicity range of $Z = (0.05, 0.4) Z_\odot$. The condensation fraction of the key elements is ~ 0.3 for silicate with progenitor stellar mass $M_{\text{AGB}} = 6 M_\odot$ and initial metallicity $Z = 0.05 Z_\odot$, and ~ 0.05 for carbon with $M_{\text{AGB}} = 3 M_\odot$ (Ventura et al. 2012). We interpolate and extrapolate their data to obtain the dust yield at the required stellar mass and metallicity, as in §2.1.

2.2.2 Dust production by SNe II

Massive stars end their lives as supernovae (SNe), and dust grains are formed in the ejecta of the SNe. The element synthesis determines the dust grains composition in stars and the mechanism of explosion (Nozawa et al. 2003). Furthermore, the reverse shock of SN destroys the dust grains by sputtering (Nozawa et al. 2007; Bianchi & Schneider 2007). Dust destruction by SN reverse shock is still under debate and there is no common agreement (e.g., Gall et al. 2014; Biscaro & Cherchneff 2016; Matsuura et al. 2019; Slavin et al. 2020), but we use Nozawa et al. (2007) as a working hypothesis in this paper. Nozawa et al. (2007) calculates the grain size distribution produced by SNe II, and we adopt it for SNe in a progenitor mass range of 13–30 M_\odot . They calculate only production by SNe II from zero-metallicity star, but the size distribution and composition of dust produced by the SNe II are less dependent on the metallicity of the progenitor stars (e.g., Todini & Ferrara 2001; Kozasa et al. 2009). Therefore, we assume that the dust production from the SN does not depend on metallicity and uses the stellar mass interpolated and extrapolated.

Nozawa et al. (2007) discusses two extreme cases for the structure of the cores of progenitor stars, mixed and unmixed. According to Hirashita et al. (2005), the unmixed model gives a better fit to the observed high- z extinction curve of SDSS J1048+4637 at $z = 6.2$ (Maiolino et al. 2004). Thus, we adopt the unmixed model in this paper. The condensation fraction is about 0.003–0.006 (Nozawa et al. 2007).

2.2.3 Dust destruction by supernova shock

Dust grains in the ISM are partially destroyed by SN shocks (e.g., Jones et al. 1996; Nozawa et al. 2006). The SN shocks decrease the total dust mass, and change the size distribution through the sputtering process (Nozawa et al. 2006). The sputtering is separated into thermal and non-thermal. The thermal sputtering is caused by the motion of hot gas, and nonthermal one is caused by relative motion between gas and dust grain. The sputterings depend on grain size, gas density, temperature (for thermal sputtering), and the relative velocity between dust grain and gas (for nonthermal sputtering).

We adopt the result by Yamasawa et al. (2011) for the treatment of the SN destruction. The grain number density after the destruction by SN shocks, $f'_X(a, t)$, is formulated as

$$f'_X(a, t) = \int_a^{a_{\text{max}}} \eta_X(a, a') f_X(a', t) da'. \quad (19)$$

Where $\eta_X(a, a')$ is the conversion efficiency of SN sputtering defined as the conversion rate of dust grains from radii $[a, a + da]$ to $[a', a' + da']$. a_{max} is the maximum radius of dust grain and we adopt $a_{\text{max}} = 8 \mu\text{m}$ (Asano et al. 2013b). This value is large enough to represent the maximum size produced by shattering and coagulation (Hirashita & Yan 2009). Yamasawa et al. (2011) calculate η_X by the method developed by Nozawa et al. (2006). In this process, the size of dust grains is only reduced by destruction, if $a > a'$, $\eta_X = 0$. Equation (19) represents the increasing amount of dust with radii $[a, a + da]$ by

SN destruction of dust larger than a . The actual upper limit of the integration corresponds to the maximum dust size of the distribution before the shock passes. The change of grain number density caused by SN shock is represented as

$$\begin{aligned} df_X(a, t) &= f'_X(a, t) - [1 - \eta_X(a, a)]f_X(a, t) \\ &= \int_0^{a_{\max}} \eta_X(a, a')f_X(a', t) da' - f_X(a, t). \end{aligned} \quad (20)$$

The change of grain mass density by SN shock at a grain radius a and the time t is represented by Eq. (20) as,

$$\begin{aligned} \left(\frac{d\rho_X(m_d, t)}{dt} \right)_{SN} &= m_d \frac{df_X(a, t)}{dt} \\ &= -\tau_{SN, X}^{-1} \left[\rho_X(m_d, t) \right. \\ &\quad \left. - m_d \int_0^{a_{\max}} \eta_X(a, a')f_X(a', t) da' \right]. \end{aligned} \quad (21)$$

If we integrate this equation with respect to a and summing up the dust species, it agrees with the third term of the right hand side of Equation (4). The timescale of dust destruction $\tau_{SN}(t)$ by SN is expressed as,

$$\tau_{SN}(t) = \frac{M_{ISM}(t)}{\epsilon m_{\text{swept}} \gamma_{SN}(t)}, \quad (22)$$

where ϵ is the efficiency of the dust destruction by SN shocks, and $\gamma_{SN}(t)$ is the SN rate. The SN rate is expressed as follows by (McKee 1989; Nozawa et al. 2006),

$$\gamma_{SN}(t) = \int_{\max(m_{\min}(t), 8 M_{\odot})}^{40 M_{\odot}} \phi(m) \text{SFR}(t - \tau_m) dm. \quad (23)$$

The integration range is determined by when the SNe can occur (Heger et al. 2003). When $t < \tau(40 M_{\odot})$, $\gamma_{SN}(t) = 0$. We assume $\epsilon = 0.1$ (McKee 1989; Nozawa et al. 2006).

m_{swept} is the ISM mass swept by a SN shock. m_{swept} depends on the density and metallicity of the ISM (Nozawa et al. 2006; Yamasawa et al. 2011). When the ISM density is high, m_{swept} is small because there are many particles that slow down the SN shock. When the metallicity is high, efficient line cooling with metal results in a faster shock deceleration and smaller m_{swept} . We use the following formulae fitted by Yamasawa et al. (2011),

$$m_{\text{swept}} = 1535 n_{SN}^{-0.202} [(Z/Z_{\odot}) + 0.039]^{-0.289} M_{\odot}, \quad (24)$$

where n_{SN} is the ISM density surrounding SNe. The fitting accuracy is within 16% for $0.03 \text{ cm}^{-3} \leq n_{SN} \leq 30 \text{ cm}^{-3}$ and for $10^{-4} \leq Z/Z_{\odot} \leq 1.0$ (Yamasawa et al. 2011), and we use $n_{SN} = 1.0 \text{ cm}^{-3}$.

2.2.4 Grain growth by metal accretion

In the cold phase of the ISM, the metal in the gas phase is accreted onto the pre-existing dust grain surface, which increases the radius of the dust grain and the total mass of the dust, known as grain growth (e.g., Dwek & Scalo 1980; Draine 2009; Jones & Nuth 2011). We assume that grain growth occurs in the CNM ($T_{\text{gas}} = 100 \text{ K}$ and $n_{\text{H}} = 30 \text{ cm}^{-3}$) and the MC ($T_{\text{gas}} = 25 \text{ K}$ and $n_{\text{H}} = 300 \text{ cm}^{-3}$). The total mass fraction in these ISM phases is assumed to be 0.5 (Nozawa et al. 2015). We treat only refractory grains (silicate and carbonaceous dust) and do not consider the icy mantle. We assume that a grain instantly becomes a sphere with a smooth surface, and we adopt only the geometric cross-section, i.e., we do not consider the effect of the Coulomb interaction. Here, we consider only two species of dust grain, carbonaceous with key element C and silicate

with Si. Jones & Nuth (2011) indicate that in an H_2 , CO and H_2O -rich environment, Si, Fe and Mg accretion forms silicates through complex chemical reactions such as ice formation. However, they also say that the spectrum of silicates formed in such a scenario is inconsistent with actual observations. In this paper, we do not know the chemical properties well, so it is assumed that only the same key element X accretes onto the dust of key elements X. Since grain growth requires a sufficient amount of metals and dust grains in the ISM, grain growth is difficult to occur in a very young galaxy, but it becomes efficiently processed at 1 Gyr in general (Asano et al. 2013a).

In the following, we introduce the formalism of size evolution by Hirashita & Kuo (2011). The collision rate at which an atom of element X with radius a with the surface of the dust grain is expressed as follows (Evans 1994):

$$\mathcal{R} = \pi a^2 n_X(t) v_{\text{th}}, \quad (25)$$

where $n_X(t)$ is the number density of the key element X in gas phase and v_{th} is the thermal velocity

$$v_{\text{th}} = \left(\frac{8kT_{\text{gas}}}{\pi m_X} \right)^{1/2}, \quad (26)$$

where k is the Boltzmann constant, T_{gas} is the gas temperature and m_X is the atomic mass of the key element X. In reality, since metals other than the corresponding key element may accrete onto the grain surface, Equation (25) represents the accretion rate associated with the key element. The evolution of grain mass $dm_d(a, t)/dt$ is

$$\frac{dm_d(a, t)}{dt} = g_X^{-1} m_d \alpha_{\text{acc}} \mathcal{R}, \quad (27)$$

where g_X is the mass fraction of the key element X in a specific grain species (silicate: 0.166, graphite: 1.00). We assume $\text{Mg}_{1.1}\text{Fe}_{0.9}\text{SiO}_4$ for the composition of silicate (Draine & Lee 1984). α_{acc} is the sticking probability of atoms that collide with grains. It is very difficult to quantify whether the sticking atoms become a part of the grain (e.g., Jones & Nuth 2011). This value may be almost 1 in the low temperature environment (e.g., Zhukovska et al. 2008), so this paper sets $\alpha_{\text{acc}} = 1$ for simplicity.

$n_X(t)$ is estimated as

$$n_X(t) = \frac{\rho_{ISM}^{\text{eff}} M_X(t) - g_X M_{d, X}(t)}{m_d M_{ISM}(t)}, \quad (28)$$

where $M_X(t)$ is the total mass of element X (including gas and dust), $M_{ISM}(t)$ is the total mass of gas, $M_{d, X}(t)$ is the dust mass associated with element X, and ρ_{ISM}^{eff} is the effective ISM mass density which is averaged mass density of the cloud where accretion process occurs. ρ_{ISM}^{eff} is calculated as $\rho_{ISM}^{\text{eff}} = \mu m_{\text{H}} n_{\text{H, acc}}$, where $\mu = 1.4$ is the mean atomic weight, m_{H} is the hydrogen atom mass, and $n_{\text{H, acc}}$ is the mean hydrogen number density in the ISM where the accretion process takes place. When $\eta = \eta_{\text{CNM}} + \eta_{\text{MC}} = 0.5$, $n_{\text{H, acc}}$ is 130 cm^{-3} . The second term on the right hand side represents the gas mass of element X to total ISM mass ratio. From (25)–(28), the grain mass growth rate is

$$\begin{aligned} \frac{dm_d(a, t)}{dt} &= \frac{\pi a^2 m_d \alpha_{\text{acc}} v_{\text{th}}}{g_X} n_X(t) \\ &= \frac{\pi a^2 \alpha_{\text{acc}} \rho_{ISM}^{\text{eff}} v_{\text{th}}}{g_X} \frac{M_X(t) - g_X M_{d, X}(t)}{M_{ISM}(t)}. \end{aligned} \quad (29)$$

The total mass growth rate by accretion process $(dM_d(t)/dt)_{\text{acc}}$ is calculated by integrating the Equation (29) with respect to the grain

radius and summing up for all dust species in all ISM phases. From Equation (17) and (29), grain radius growth rate is represented as

$$\frac{da}{dt} = \frac{\alpha_{\text{acc}} \rho_{\text{ISM}}^{\text{eff}} v_{\text{th}} M_X(t) - g_X M_{d,X}(t)}{4s g_X M_{\text{ISM}}(t)}. \quad (30)$$

In computation, we solve this equation for each size bin at each time step. By transferring all the dust that was in the radius bin before metal accretion to the radius bin after accretion, the evolution of size distribution by metal accretion can be calculated. The number of dust grains does not change in this process.

2.2.5 Grain-grain collision

We consider two types of grain-grain collisions, shattering, and coagulation. They only change dust size distribution and conserve total grain mass in the ISM. Which processes occur is determined by the relative velocity between two collisional grains. In the case that the relative velocity is fast, shattering is easy to occur. On the contrary, when the relative velocity is small, coagulation occurs. Relative velocities between dust grains can be caused by ubiquitous ISM turbulence (e.g., [Draine & Anderson 1985](#); [Ossenkopf 1993](#); [Lazarian & Yan 2002](#); [McKee & Ostriker 2007](#); [Hirashita & Yan 2009](#); [Ormel et al. 2009](#)). Furthermore, because the dust is thought to be magnetized ([Arons & Max 1975](#)), it is necessary to consider the motion of grains due to magnetohydrodynamics (MHD) turbulence. We consider dust collisions by applying the relative velocity of grains in MHD turbulence calculated by [Yan et al. \(2004\)](#). The velocity is calculated in consideration of gas drag (hydro drag) and gyroresonance. When a grain with a relative velocity higher than the threshold collides, it is shattered into small pieces. Since the larger grains are affected by turbulence strongly, they have a large relative velocity and it can occur shattering. [Yan et al. \(2004\)](#) indicate that grains with $a > 10^{-6}$ cm can accelerate to velocity ($1\text{--}2 \text{ km s}^{-1}$) close to the shattering threshold in CNM. In WNM, gyroresonance accelerates grain with $a > 2\text{--}3 \times 10^{-5}$ cm to high relative velocity ($\sim 20 \text{ km s}^{-1}$). On the contrary, small dust has a small relative velocity and causes coagulation. When the relative velocity is small, the collision cross section is small, so a high density environment (e.g., MC) is required for coagulation. We consider silicate and graphite as grain species while grain-grain collision, and they collide only with the same species. Furthermore, we treat spherical grains which have a constant density. [Hirashita & Yan \(2009\)](#) calculates in various ISM phases (including CNM, WNM, and MC) by shattering and coagulation, and the Asano model applied the same method.

We consider four types of grain-grain collisions, in other words, the relative velocity is divided into four types. This treatment is the same as [Jones et al. \(1994\)](#) and [Hirashita & Yan \(2009\)](#). Considering the shattered and coagulated grains are radii a_1 and a_2 , which are called grain 1 and 2, respectively. The mass of grain 1 and 2 is denoted as m_1 and m_2 . The relative collisional velocities between grain 1, and 2 are as follows,

- front collision ($v_{1,2} = v_1 + v_2$)
- back-end collision ($v_{1,2} = |v_1 - v_2|$)
- side collision ($v_{1,2} = v_1$)
- another side collision ($v_{1,2} = v_2$)

where v_1 and v_2 are the velocity of grain with radii a_1 and a_2 , respectively. We assume that collisions in all directions have the same probability.

[Jones et al. \(1996\)](#) suggests that the shattering is significantly affecting the grain size distribution in the ISM. The time evolution

of grain mass density by shattering process is

$$\begin{aligned} \left[\frac{d\rho_X(m_d, t)}{dt} \right]_{\text{shat}} &= -m_d \rho_X(m_d, t) \\ &\times \int_{a_{\min}}^{a_{\max}} \alpha[m_d, m_1] \rho_X(m_1, t) dm_1 \\ &+ \int_{a_{\min}}^{a_{\max}} \int_{a_{\min}}^{a_{\max}} \alpha[m_1, m_2] m_{\text{shat}}^{1,2}(m_d) \\ &\times \rho_X(m_1, t) \rho_X(m_2, t) dm_1 dm_2, \end{aligned} \quad (31)$$

where $\alpha[m_1, m_2]$ is the collision frequency normalized by two grain masses and grain number density and expressed as

$$\alpha[m_1, m_2] = \begin{cases} 0 & (v_{1,2} < v_{\text{shat}}) \\ \frac{\sigma_{1,2} v_{1,2}}{m_1 m_2} & (v_{1,2} > v_{\text{shat}}) \end{cases}, \quad (32)$$

$m_{\text{shat}}^{1,2}(m_d)$ represents the total mass of fragments with masses between m_d and $m_d + dm_d$ as the result of collision between grain 1 and 2. We assume that the distribution of shattered fragments is proportional to $a^{-3.3}$ ([Hellyer 1970](#); [Jones et al. 1996](#)). σ is the collisional cross-section and represented as

$$\sigma_{1,2} = \beta \pi (a_1 + a_2)^2, \quad (33)$$

β is the coefficient connecting the cross-section and the geometric cross-section, assumed $\beta = 1$ for simplicity. v_{shat} is the threshold of shattering, we assume 1.2 km s^{-1} and 2.7 km s^{-1} for silicate and graphite grains, respectively ([Jones et al. 1996](#)). a_{\min} and a_{\max} are minimum and maximum radius and we adopt $a_{\min} = 0.0003 \mu\text{m}$ and $a_{\max} = 8 \mu\text{m}$, respectively ([Asano et al. 2013b](#)). The minimum grain radius in the ISM is less well understood, even if $a_{\min} = 0.001 \mu\text{m}$, the dust size distribution does not change significantly ([Hirashita 2012](#)).

The first term on the right hand side of Equation (31) represents the decrease of grain mass m_d due to destruction by the collisions with other grains. The second term represents the grain mass m_d increase due to the fragments resulting from the collision between grain 1 and 2. Shattering does not produce larger fragments than the original grain, so it only contributes if either grain 1 or 2 is heavier than m_d .

The coagulation occurs when the relative velocity is low. The time evolution for coagulation is expressed as a similar form to shattering,

$$\begin{aligned} \left[\frac{d\rho_X(m_d, t)}{dt} \right]_{\text{coag}} &= -m_d \rho_X(m_d, t) \\ &\times \int_{a_{\min}}^{a_{\max}} \alpha[m_d, m_1] \rho_X(m_1, t) dm_1 \\ &+ \int_{a_{\min}}^{a_{\max}} \int_{a_{\min}}^{a_{\max}} \alpha[m_1, m_2] m_{\text{coag}}^{1,2}(m_d) \\ &\times \rho_X(m_1, t) \rho_X(m_2, t) dm_1 dm_2. \end{aligned} \quad (34)$$

and

$$\alpha[m_1, m_2] = \begin{cases} \frac{\sigma_{1,2} v_{1,2}}{m_1 m_2} & (v_{1,2} < v_{\text{coag}}) \\ 0 & (v_{1,2} > v_{\text{coag}}) \end{cases}, \quad (35)$$

where $m_{\text{coag}}^{1,2}$ is the total mass of coagulated grains:

$$m_{\text{coag}}^{1,2}(m_d) = \begin{cases} m_d & \text{when } m_d \leq m_1 + m_2 < m_d + dm_d \\ 0 & \text{otherwise} \end{cases}. \quad (36)$$

We use Equation (33) as the collisional cross-section for coagulation. v_{coag} is the threshold velocity of coagulation, and grains with higher relative velocity do not stick. [Chokshi et al. \(1993\)](#) calculate the

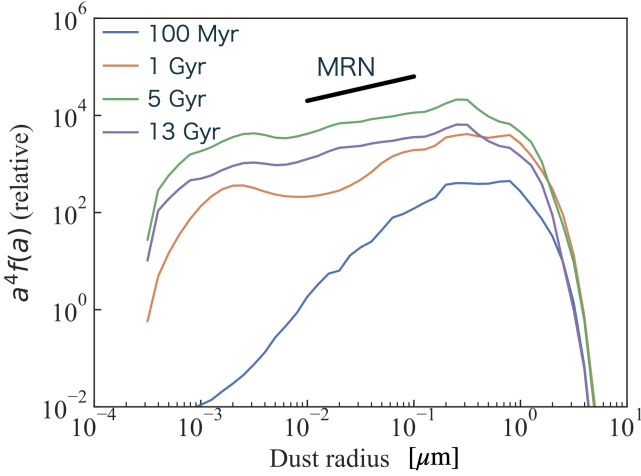


Figure 1. The time evolution of all species of dust grain size distribution. Blue, orange, green, and purple curves indicate the age of 100 Myr, 1 Gyr, 5 Gyr, and 13 Gyr, respectively. Black line represents the slope of the MRN distribution.

threshold velocity as 10^{-3} – 10^{-1} km s $^{-1}$ and it depends on the grain size. Here we assume that the dust grain is a smooth sphere, but in the real picture the grain is fluffy (Ossenkopf 1993). It has been suggested that the coagulation threshold relative velocity is higher because fluffiness increases the cross-section of grain collisions (Ormel et al. 2009; Hirashita & Kobayashi 2013). In addition, Asano et al. (2014) indicate that the coagulation threshold suppresses the production of large grain, producing smaller grain ($a < 0.01$ μm) than the Mathis et al. (1977). Therefore, in this paper, it is assumed that coagulation can occur at all relative velocities without setting the coagulation threshold. The first term of Equation (34) indicates the decrease of the grain with mass m_d by coagulation with other grains. The second term indicates the increase of the grain with mass m_d by coagulation between grain 1 and 2. Since coagulation works effectively on small size dust, it becomes effective after shattering becomes effective and small dust increases. Coagulation shifts the dust size distribution to the larger one.

2.2.6 Result of dust evolution model

We show the dust grain (including carbon and silicate) size distribution calculated with the star formation timescale $\tau_{SF} = 3$ Gyr and total galaxy mass $10^{11} M_{\odot}$ in Figure 1. We note that the total galaxy mass is merely a normalization for our dust model, and can be rescaled freely.

In this representation, the ratio of ISM phases are $\eta_{WNM} = 0.5$, $\eta_{CNM} = 0.3$, $\eta_{MC} = 0.2$. Blue, orange, green, and purple curves indicate the age of 100 Myr, 1 Gyr, 5 Gyr, and 13 Gyr, respectively. Black curve indicates the slope of the grain size distribution suggested by Mathis et al. (1977) which reproduces the MW extinction curve. This is known as the MRN distribution, expressed by a single power law,

$$f(a)da \propto a^{-3.5}da \quad (0.005 \mu\text{m} < a < 0.25 \mu\text{m}). \quad (37)$$

The overview of the time evolution of dust size distribution is as follows.

- < 100 Myr

- Dust production from SNe dominates, and the original size distribution of SN dust is reflected in the overall dust size distribution.

- 100 Myr–1 Gyr

- Metal accretion dominates the evolution of dust.
- Shattering and coagulation become effective, and consequently dust mass rapidly increases because of the increase of the total surface area per dust mass.
- Production of PAHs is dominated by shattering.

- 1–5 Gyr

- Shattering and coagulation become more effective.
- Metal accretion also becomes more effective thanks to the increased amount of small dust continuously generated by shattering.
- The increase of dust mass is the most rapid between 1 Gyr and 2 Gyr.

- 5–13 Gyr

- The production of dust grain by stars decreases, and shattering and coagulation dominate the evolution of the grain size distribution.

Details of each step in the evolution of dust size distribution is explained as follows. At the age of 100 Myr, only a tiny amount of grains exist in the ISM, and the slope of size distribution is completely different from the slope of the MRN distribution. Particularly, PAHs are not produced in early galaxies. Figure 2 shows how different processes (i.e., production by AGB and SNe, and grain growth in the ISM) contribute to the increase of the total PAH mass. We note that the contribution of destruction processes including the SN shock and astration are not shown here. The dust destruction process only depends on the grain size and species, then it works in the same way for dust from any production source. Therefore, even if dust reduction is taken into account, the ratio of dust mass for each source remains the same. In galaxies younger than 100 Myr, short-lived SNe II (lifetime $\sim 10^6$ – 10^7 yr) is the main source of dust supply (e.g., Maiolino et al. 2004; Hiraki & Hirak 2008), as the age of the galaxy is too young for stars to evolve into AGB (lifetime $\sim 10^8$ – 10^9 yr) (e.g., Morgan & Edmunds 2003; Marchenko 2006). However, smallest grains such as PAHs are supplied from SN stars, though the amount is very small (e.g., Nozawa et al. 2007). As the chemical evolution proceeds in the galaxy, the amount of metal in the ISM increases. Very young galaxies (age ≈ 20 Myr) have only a small supply of dust from SNe. When the galaxy age reaches ~ 100 Myr, the smallest grains (PAH) are gradually formed by shattering, and the mass of the PAH increases. The galaxy must evolve to reach the critical metallicity for dust growth to work effectively (Inoue 2011; Asano et al. 2013a). Since AGB provides larger size dust grains (> 0.1 μm), their contribution to PAHs is not significant (Winters et al. 1997; Yasuda & Kozasa 2012).

At 1 Gyr, the total dust mass continues to increase gradually, while the PAH mass starts to increase significantly, because the shattering in the ISM becomes effective. The bump in 10^{-3} – 10^{-2} μm in Figure 1 is the consequence of the activated shattering process. We show the evolution of the total dust mass of the model galaxy in Figure 3. Solid and dashed lines represent the dust grain evolution in the ISM (fiducial) and without evolution (no evolution) case, respectively. Figure 3 clearly demonstrates that, if dust grains evolve in the ISM, dust mass rapidly increases by metal accretion in 1–2 Gyr. It has been suggested that in the MW-like galaxy model, when the metallicity

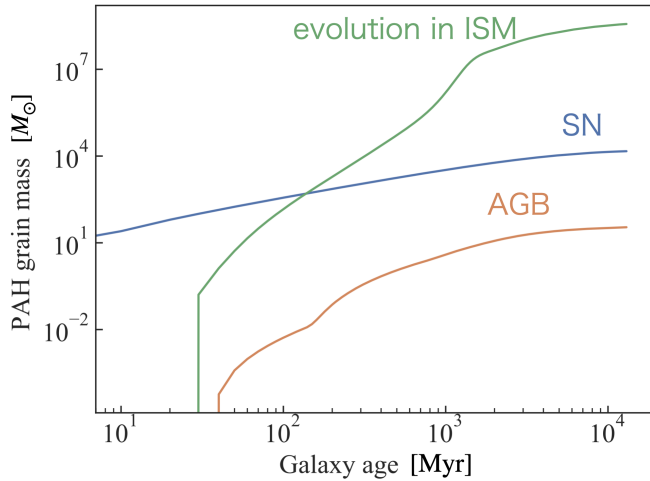


Figure 2. The evolution of PAH mass per each production source. The total galaxy mass is $10^{11} M_{\odot}$. Blue, orange, and green curves represent PAH mass produced by SN, AGB, and evolution in the ISM, respectively.

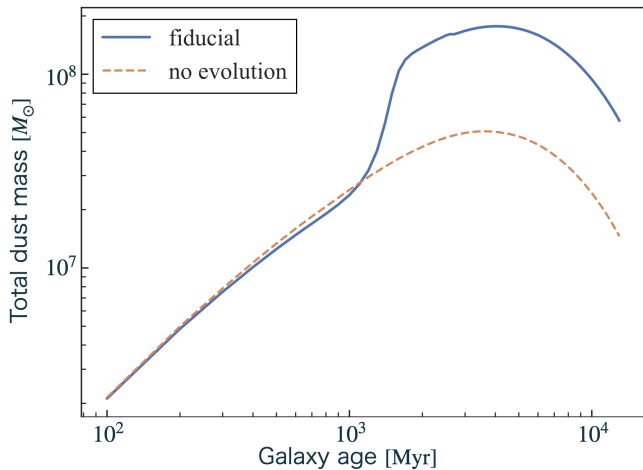


Figure 3. The evolution of dust to gas mass ratio calculated by the Asano model.

exceeds $0.1 Z_{\odot}$, the metal accretion process becomes effective and the dust mass drastically increases (Asano et al. 2013a). When the metal accretion becomes effective, dust collisions with each other in the ISM become more likely to occur, and the shattering and coagulation also become effective. The shattering process results in a significant increase in the amount of small dust grains including PAH. Since the metal accretion depends on the total surface area of dust grain (Equation (25)), the shattering promotes the accretion. Such a dust growth cycle causes the dust mass to increase nonlinearly. This cycle is effective between 1 Gyr and 2 Gyr in this model galaxy.

After that, the mass of dust increases and peaks at ~ 3 Gyr. This peak time depends on the timescale of star formation $\tau_{\text{SF}} = 3$ Gyr. After 3 Gyr, the dust mass decreases due to the destruction by SN shocks. The smaller the dust size, the more effectively the SN destruction works (Nozawa et al. 2006). In addition, production of dust from stars also decreases due to the decrease of the SFR. Thus, in total, the dust mass gradually decreases by SN shock and astration. As the production of dust by stars decreases, coagulation dominates

the evolution of dust size distribution. Due to the SN shock destruction and coagulation, the dust size distribution is biased toward larger radius. For galaxies with fully grown dust after 5 Gyr, the dust grain size distribution finally converges to a similar function to that obtained from observations of nearby galaxies such as Schurer et al. (2009). A galaxy with the age in 5–13 Gyr has a dust distribution with a power-law slope similar to the MRN.

In contrast, for the no evolution case, the total grain mass does not increase rapidly and only increases by stellar production with a constant rate up to $\tau_{\text{SF}} = 3$ Gyr. In the age of the < 1 Gyr galaxy, no evolution case has a larger grain mass than the mass of the fiducial case. This is because the no evolution case does not consider the destruction of dust due to SN shocks. After 3 Gyr, the dust mass decreases by astration. As described above, if the evolution of dust in the ISM is not taken into account in the calculation, a rapid increase of dust mass in 1–2 Gyr does not appear.

2.3 Stellar SED

We use the version 2 of PÉGASE (Fioc & Rocca-Volmerange 1999, PÉGASE.2) to produce stellar SEDs. PÉGASE calculates the stellar emission by stellar population synthesis (SPS) method with simple stellar populations (SSPs). The SSP represents the time variation of the SED of a single contemporaneous stellar population with a single metallicity and abundance pattern. The monochromatic luminosity per unit wavelength of SSP is expressed as

$$L_{\lambda}^{\text{SSP}}(t, Z) = \int_{m_{\text{min}}}^{m_{\text{max}}} L_{\lambda}^{\text{star}}(T_{\text{eff}}(t, m), \log g(t, m), Z) \phi(m) dm, \quad (38)$$

where $L_{\lambda}^{\text{star}}$ is the monochromatic luminosity of a star with the mass in the interval effective temperature T_{eff} , surface gravity of stellar g , metallicity Z , and an age of galaxy t (e.g., Conroy 2013). m_{max} and m_{min} are the upper and lower limit of stellar mass, set to be $100 M_{\odot}$ and $0.1 M_{\odot}$, which is the same as the IMF integration range. The effective temperature $T_{\text{eff}}(t, m)$ and the surface gravity $\log g(t, m)$ are from the stellar evolutionary track. PÉGASE.2 uses the evolutionary track based on the Padova tracks (Bressan et al. 1993; Fagotto et al. 1994b,c,a; Girardi et al. 1996). The metallicity of the ISM Z evolves with galaxy age t and it is calculated from Woosley & Weaver (1995) SN II models. Since only the evolutionary track table with metallicities $Z = (0.005, 0.02, 0.2, 0.4, 1, 0, 2.5, 5.0) Z_{\odot}$ is prepared, they use the interpolated value. PÉGASE assumes that a star releases metal into ISM only at the end of its life, and the recycling model is not instantaneous. The library of stellar spectra used by PÉGASE.2 is divided into two according to effective temperature T_{eff} . For $T_{\text{eff}} < 50000$ K, the library comes from Lejeune et al. (1997, 1998, corrected version (BaSeL-2.0)).

A monochromatic luminosity from total stars at time t is calculated by weighting L_{λ}^{SSP} at galaxy age t' with star formation rate SFR,

$$L_{\lambda}(t) = \int_{t'=0}^{t'=t} \int_{Z=0}^{Z=Z_{\text{max}}(t-t')} \text{SFR}(t-t') L_{\lambda}^{\text{SSP}}(t', Z(t-t')) dZ dt', \quad (39)$$

where $Z_{\text{max}}(t-t')$ is the maximum metallicity at time $t-t'$. In order to take into account the stars that were born at the time of the galaxy's birth to the stars that are just born, the value is integrated over time. The time lag $t-t'$ represents the time difference between the formation of a star and the end of the evolution of the star. We chose the Schmidt law (Schmidt 1959, Equation (5)) for the SFR.

2.4 Dust properties

Radiative transfer is the method to calculate the propagation of energy in systems of various sizes (from isolated gas clouds to galaxies). In the galaxy ISM, radiation is mainly affected by absorption and scattering by dust grains. One of the easiest ways to calculate radiative transfer is to assume that the ISM has a homogeneous distribution. However, it has been observed that actual galaxies have a more complex structure in general (e.g., Field et al. 1969; McKee & Ostriker 1977). If a homogeneous dust distribution is assumed, the optical depth of the dust is larger than that in the case of inhomogeneous distribution. In other words, if the dust mass is estimated with a homogeneous distribution, the attenuation per dust grain is overestimated, and the dust mass would be underestimated as a consequence. Therefore, in this paper, we consider a clumpy dust distribution.

The calculation of three-dimensional radiative transfer with clumpy dust usually requires substantial computational cost. Neufeld (1991) and Hobson & Padman (1993) introduced the method that solves the radiative transfer with MGA in a one-dimensional plain parallel galaxy (Varosi & Dwek 1999; Inoue 2005). The MGA treats the dusty region as a kiloparsec-size huge grain called mega-grain, and regards absorption and scattering behave in the same way as typical grains with effective optical properties. We approximate the complex distribution of stars, dust grains, and gas in the model galaxy, to simplify costly calculations in three-dimensional space. In this approximation, the distribution of young stars is clumpy and the young stars are embedded by mega-grain. In contrast, old stars are supposed to distribute smoothly in a diffuse way. The light emitted by young stars is stronger attenuated than the light emitted by older stars due to the surrounding mega-grains. Inoue (2005) researched the effect of changing criterion of young star t_y . He conclude 10 Myr is best fit to the MW attenuation, and we apply it in this paper. Assuming thermal and chemical equilibrium with temperature $T < 10^4$ K, the ISM is represented by two phases, WNM and CNM (e.g., Wolfire et al. 2003; Koyama & Inutsuka 2002). The relation of the thermal pressure with hydrogen density is expressed by fitting the phase diagram (Inoue 2005) as,

$$\frac{p/k}{10^4 \text{ K cm}^{-3}} = \frac{n_{\text{H,WNM}}}{1 \text{ cm}^{-3}}, \quad (\text{WNM}) \quad (40)$$

$$\frac{p/k}{10^{4.5} \text{ K cm}^{-3}} = \left(\frac{n_{\text{H,CNM}}}{10^3 \text{ cm}^{-3}} \right)^{0.7}, \quad (\text{CNM}) \quad (41)$$

where p is the pressure. $n_{\text{H,WNM}}$ and $n_{\text{H,CNM}}$ are the hydrogen density of WNM and CNM, respectively. We regard the WNM as a homogeneous interclump medium and the CNM as a clump. The clump radius r_{cl} is calculated by assuming it to be self-gravitating (Inoue 2005),

$$r_{\text{cl}} = \frac{1}{\rho_{\text{cl}}} \sqrt{\frac{15p}{4\pi G}} = \frac{1}{\mu m_{\text{p}} n_{\text{H,CNM}}} \sqrt{\frac{15p}{4\pi G}} \sim 10.4 \text{ pc}, \quad (42)$$

where $\rho_{\text{cl}} = \mu m_{\text{p}} n_{\text{H,CNM}}$ is the clump density, μ is the mean atomic density, G is the gravitational constant and m_{p} is the proton mass. Clumps exist in the interclump medium. We assume all clumps are spherical and have a constant radius and density. In this approximation, we use the mass absorption and scattering coefficient and the scattering asymmetry parameter of dust grain, k_{abs} , k_{scat} and g_{d} respectively, averaged by dust size distribution calculated by the Asano

model:

$$k_{\text{abs}} = \frac{\int_{a_{\text{min}}}^{a_{\text{max}}} \pi a^2 Q_{\text{abs}}(a) f(a) da}{\int_{a_{\text{min}}}^{a_{\text{max}}} m_{\text{d}}(a) f(a) da}, \quad (43)$$

$$k_{\text{scat}} = \frac{\int_{a_{\text{min}}}^{a_{\text{max}}} \pi a^2 Q_{\text{scat}}(a) f(a) da}{\int_{a_{\text{min}}}^{a_{\text{max}}} m_{\text{d}}(a) f(a) da}, \quad (44)$$

$$g_{\text{d}} = \frac{\int_{a_{\text{min}}}^{a_{\text{max}}} g(a) \pi a^2 Q_{\text{scat}}(a) f(a) da}{\int_{a_{\text{min}}}^{a_{\text{max}}} \pi a^2 Q_{\text{scat}}(a) f(a) da}, \quad (45)$$

where $f(a)$ is the dust number distribution, $Q_{\text{abs}}(a)$ and $Q_{\text{scat}}(a)$ are the absorption and scattering coefficient, and $g(a)$ is the scattering asymmetry parameter of a grain, respectively. In this model $Q_{\text{abs}}(a)$, $Q_{\text{scat}}(a)$, and $g(a)$ are calculated by the Mie theory (Bohren & Huffman 1983). We adopt Draine & Lee (1984) and Laor & Draine (1993) for silicate and graphite, and Li & Draine (2001) for PAH as optical parameters. The mass extinction coefficient and scattering albedo are defined as

$$k_{\text{d}} = k_{\text{abs}} + k_{\text{scat}}. \quad (46)$$

In the MGA, we replace the optical properties, namely the extinction coefficient per unit length κ , the scattering albedo ω , and the scattering asymmetry parameter g with the effective ones. The relative optical depth of a clump with the interclump medium is

$$\tau_{\text{cl}} = (\rho_{\text{cl}} - \rho_{\text{icm}}) k_{\text{d}} D r_{\text{cl}}. \quad (47)$$

where D is the dust-to-gas mass ratio calculated by the Asano model. The extinction coefficient per unit length of the medium by clump is

$$\kappa_{\text{mg}} = n_{\text{cl}} \pi r_{\text{cl}}^2 P_{\text{int}}(\tau_{\text{cl}}) = \frac{3f_{\text{cl}}}{4r_{\text{cl}}} P_{\text{int}}(\tau_{\text{cl}}), \quad (48)$$

where n_{cl} is the number density of clump and f_{cl} is the clump filling fraction,

$$f_{\text{cl}} = \frac{n_{\text{H}} - n_{\text{H,WNM}}}{n_{\text{H,CNM}} - n_{\text{H,WNM}}}. \quad (49)$$

We assume that mean hydrogen number density in the galaxy n_{H} has a constant value 1 cm^{-3} . $P_{\text{int}}(\tau)$ is the interaction probability against parallel light by a sphere with optical depth τ , and represented as

$$P_{\text{int}}(\tau) = 1 - \frac{1}{2\tau^2} + \left(\frac{1}{\tau} + \frac{1}{2\tau^2} \right) e^{-2\tau}. \quad (50)$$

This equation is obtained by integrating the light incident on the sphere in all directions and taking the ratio to the case where the optical depth of the sphere is zero (see appendix C of Varosi & Dwek (1999) for details). The extinction coefficient of interclump medium is

$$\kappa_{\text{icm}} = k_{\text{d}} D \rho_{\text{icm}}. \quad (51)$$

Thus, the effective extinction coefficient is expressed as

$$\kappa_{\text{eff}} = \kappa_{\text{mg}} + \kappa_{\text{icm}}. \quad (52)$$

The scattering albedo of clump is

$$\omega_{\text{cl}} = \omega_{\text{d}} P_{\text{esc}}(\tau_{\text{cl}}, \omega_{\text{d}}), \quad (53)$$

where $\omega_{\text{d}} = k_{\text{scat}}/k_{\text{d}}$ is the scattering albedo of normal grain averaged by grain size distribution and

$$P_{\text{esc}}(\tau, \omega) = \frac{\frac{3}{4\tau} P_{\text{int}}(\tau)}{1 - \omega \left[1 - \frac{3}{4\tau} P_{\text{int}}(\tau) \right]}, \quad (54)$$

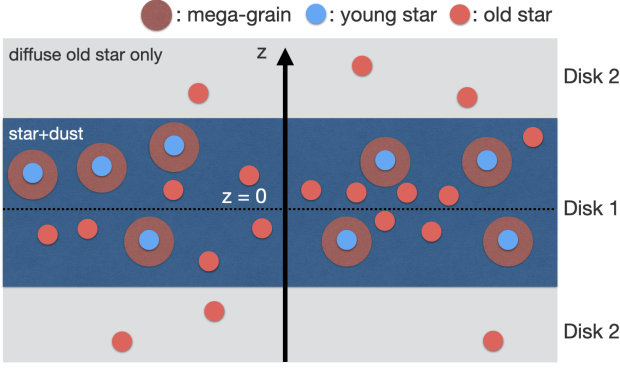


Figure 4. The geometry of a one-dimensional plain parallel galaxy.

is the photon escape probability from a sphere grain. The effective scattering albedo is

$$\omega_{\text{eff}} = \frac{\omega_{\text{cl}}\kappa_{\text{mg}} + \omega_{\text{d}}\kappa_{\text{icm}}}{\kappa_{\text{eff}}}. \quad (55)$$

The light entering the clump is scattered by the dust in the clump and escapes in various directions. An optical parameter that indicates in which direction light escapes is called an asymmetry parameter of clump and it is defined as $g_{\text{cl}} = \langle \cos \theta_{\text{esc}} \rangle$, where θ_{esc} is the angle between enter and escape directions. g_{cl} is given by fitting the Monte Carlo calculation result in [Varosi & Dwek \(1999\)](#), and represented by the following empirical formula,

$$g_{\text{cl}}(\tau_{\text{cl}}, \omega_{\text{cl}}, g_{\text{d}}) = g_{\text{d}} - C \left(1 - \frac{1 + e^{-B/A}}{1 + e^{(\tau_{\text{cl}} - B)/A}} \right), \quad (56)$$

where

$$A \equiv 1.5 + 4g_{\text{d}}^3 + 2\omega_{\text{d}}\sqrt{g_{\text{d}}}\exp(-5g_{\text{d}}), \quad (57)$$

$$B \equiv 2 - g_{\text{d}}(1 - g_{\text{d}}) - 2\omega_{\text{d}}g_{\text{d}}, \quad (58)$$

$$C \equiv \frac{1}{3 - \sqrt{2g_{\text{d}} - 2\omega_{\text{d}}g_{\text{d}}(1 - g_{\text{d}})}}. \quad (59)$$

The effective asymmetry parameter is

$$g_{\text{eff}} = \frac{g_{\text{cl}}\kappa_{\text{mg}} + g_{\text{d}}\kappa_{\text{icm}}}{\kappa_{\text{eff}}}. \quad (60)$$

2.5 Radiative transfer in a one-dimensional galaxy

We assume a one-dimensional plane-parallel galaxy along the z -axis for solving radiative transfer shown in Figure 4. We set two kinds of disks in the model. One is a gas+dust disk containing young stars (disk 1). Stars are born in cold, dense regions (CNM), so we assume young stars are surrounded by clumps, and disk 1 is also full of interclump medium. Disk 1 has a constant density of stars, gases, and grains. Optical depth τ is defined with constant effective extinction coefficient κ_{eff} as

$$d\tau = -\kappa_{\text{eff}} dz, \quad (61)$$

with $\tau = 0$ at $z = h_{\text{d}}$ and $\tau = \kappa_{\text{eff}}h_{\text{d}}$ at $z = 0$. Where $2h_{\text{d}}$ is the thickness of disk 1. The other disk contains only exponentially and smoothly distributed old stars (disk 2). The thickness of the disk 2 is $4h_{\text{d}}$, which is twice larger than that of disk 1. These two disks

are stacked so that their centers are aligned. In the above condition, radiative transfer is formulated as,

$$\mu \frac{dI(\tau, \mu)}{d\tau} = -I(\tau, \mu) + S(\tau, \mu), \quad (62)$$

where $I(\tau, \mu)$ is the specific intensity at τ and $\mu \equiv 1/\cos \theta$. The θ is the angle between the ray and z -axis. Source function S is represented as

$$S(\tau, \mu) = \frac{\eta_*(\tau)}{\kappa_{\text{eff}}} + \omega_{\text{eff}} \int_{-1}^1 I(\tau, \mu') \Phi(g_{\text{eff}}, \mu, \mu') d\mu', \quad (63)$$

where η_* is the stellar emissivity and Φ is the scattering phase function. Here we adopt the Henyey-Greenstein phase function ([Henyey & Greenstein 1941](#))

The first term in the right hand side of Equation (63) represents the intensity of light emitted from the star that escapes from the clump where the star was born. The second term in the right hand side represents the integral of the light scattered in the considering direction μ among the scattered light by dust grain. The boundary conditions in this galaxy at $z = 0$ and $z = h_{\text{d}}$ are

$$I(\tau = \kappa_{\text{eff}}h_{\text{d}}, \mu) = I(\tau = \kappa_{\text{eff}}h_{\text{d}}, -\mu), \quad (64)$$

$$I(\tau = 0, \mu < 0) = -\frac{\int_{h_{\text{d}}}^{\infty} \eta_*(z) dz}{\mu}. \quad (65)$$

The stellar emissivity is normalized by

$$\int_{-\infty}^{\infty} \eta_*(z) dz = 1. \quad (66)$$

The intrinsic emissivity from young stars in disk 1 η_*^{young} is $1/2h_{\text{d}}$ for $|z| \leq h_{\text{d}}$ and zero for $|z| > h_{\text{d}}$ because it is normalized by Equation (66). The energy emitted by young star is absorbed by the dust in clump surrounding the star. Since the escape probability from the clump is Equation (54), the emissivity from young stars is represented as

$$\eta_*^{\text{young}} \begin{cases} P_{\text{est}}(\tau_{\text{cl}}, \omega_{\text{cl}})/2h_{\text{d}} & (|z| \leq h_{\text{d}}) \\ 0 & (|z| > h_{\text{d}}) \end{cases}. \quad (67)$$

The old stars in disk 2 are distributed with exponential diffusion along the z -axis. From the normalization Equation (66), the emissivity from the old stars is

$$\eta_*^{\text{old}}(z) = \frac{e^{-|z|/2h_{\text{d}}}}{4h_{\text{d}}}. \quad (68)$$

The total stellar emissivity at z is represented as

$$\eta_*(z) = f_{\text{y}}(t)\eta_*^{\text{young}}(z) + (1 - f_{\text{y}}(t))\eta_*^{\text{old}}(z), \quad (69)$$

where $f_{\text{y}}(t)$ is the luminosity fraction emitted by young stellar at age t , it is calculated by

$$f_{\text{y}}(t) = \frac{\int_0^{\min[t_{\text{y}}, t]} \int_0^{Z_{\text{max}}(t-t')} \text{SFR}(t-t') L_{\lambda}^{\text{SSP}}(t', Z(t-t')) dZ dt'}{L_{\lambda}(t)}. \quad (70)$$

In the radiative transfer calculation, we calculate Equation (62) and (63) iteratively until the ratio to the previous loop of the source function in all directions on the galaxy surface converged to 10^{-10} .

2.6 Dust temperature distribution

The UV and optical photons emitted by stars heat dust grains. The heated dust grains release the energy by emission from MIR to FIR

wavelength photons. Large grains have an equilibrium temperature determined by the stellar radiation field. In contrast, very small grains cannot establish radiative equilibrium, and it does not have a stable equilibrium temperature (Draine & Anderson 1985; Draine & Li 2001; Li & Draine 2001; Takeuchi et al. 2003, 2005; Horn et al. 2007). Since they have small heat capacities, they are easily heated by photons and then rapidly cooled. Thus, the (instantaneous) temperature of very small grains is inevitably stochastic, we calculate temperature distribution by Monte Carlo simulation.

2.6.1 Stochastic heating

The rate at which a dust grain absorbs photons in the energy range $[E, E + dE]$ and time interval $[t, t + dt]$ is expressed as

$$d\rho(a, \lambda) = \pi a^2 Q_{\text{abs}}(a, \lambda) \bar{u}_\lambda \frac{\lambda^3}{h_p^2 c} dE dt, \quad (71)$$

where \bar{u}_λ is the mean energy density per wavelength in a galaxy, h_p is the Planck constant, and c is the speed of light, respectively (e.g., Draine & Anderson 1985; Takeuchi et al. 2003, 2005). The energy density actually varies depending strongly on its spatial position in a galaxy. Therefore, considering the different energy densities for each position, the calculation time becomes enormous. Thus, we use the mean energy density \bar{u}_λ which is calculated in the same way as Floc & Rocca-Volmerange (2019):

$$L_\lambda^0 - L_{\text{obs}} = c \bar{u}_\lambda k_{\text{abs}} M_d, \quad (72)$$

where L_λ^0 and L_{obs} are the intrinsic stellar luminosity and observed luminosity calculated by transfer radiation. Therefore, the mean energy density is represented as

$$\bar{u}_\lambda = \frac{L_\lambda^0 - L_{\text{obs}}}{c k_{\text{abs}} M_d}. \quad (73)$$

Equation (71) can be regarded as the probability density distribution if the time interval dt is appropriately small. For each dust size, dt is determined so that the maximum collision probability among all wavelengths is 0.01,

$$dt(a) = 0.01 \left[\pi a^2 Q_{\text{abs}}(a, \lambda) \bar{u}_\lambda \frac{\lambda^3}{h_p^2 c} dE \right]^{-1}. \quad (74)$$

For simplicity, we assume that the energy of an absorbed photon is totally used to heat the dust grains, represented as

$$E(T + \Delta T) = E(T) + \frac{h_p c}{\lambda}, \quad (75)$$

where $E(T)$ is the enthalpy of dust grains at temperature T and ΔT is the increment of temperature. We adopt the Debye model for calculating the enthalpy of dust grains (Li & Draine 2001). The enthalpy of silicate and graphite grains are

$$E_{\text{sil}}(T) = (N_{\text{atom}} - 2)k \left[2f_2 \left(\frac{T}{500 \text{ K}} \right) + f_3 \left(\frac{T}{1500 \text{ K}} \right) \right], \quad (76)$$

$$E_{\text{gra}}(T) = (N_C - 2)k \left[f_2 \left(\frac{T}{863 \text{ K}} \right) + 2f_2 \left(\frac{T}{2504 \text{ K}} \right) \right], \quad (77)$$

where

$$f_n(a) \equiv n \int_0^1 \frac{y^n dy}{\exp(y/x) - 1}. \quad (78)$$

The subscripts 'sil' and 'gra' represent the silicate and graphite

grains, respectively. Equation (78) is the n dimensional Debye function. N_{atom} and N_C are the number of atoms in a grain, they are expressed as,

$$N = \frac{4}{3} \pi a^3 \rho N_A / M, \quad (79)$$

where ρ is the mass density, M is the mass number and N_A is the Avogadro constant. For carbonaceous (graphite or PAH) grain, $\rho = 2.26 \text{ g/cm}^3$ and $M = 12.0 \text{ g/mol}$ (Draine & Lee 1984). For silicate grain, $\rho = 3.50 \text{ g/cm}^3$ and $M = 172.25 \text{ g/mol}$ (Li & Draine 2001). In polycyclic aromatic hydrocarbon (PAH) grains, we consider C-C bond modes are same as graphite and C-H bond modes component is added to Equation (77),

$$E_{\text{pah}}(T) = E_{\text{gra}} + \frac{H}{C} N_C \sum_{j=1}^3 \left(\frac{h_p \nu_j}{\exp(h_p \nu_j / kT) - 1} \right). \quad (80)$$

The index j represents the C-H out-of-plane bending modes ($\nu_1/c = 886 \text{ cm}^{-1}$), in-plane bending modes ($\nu_2/c = 1161 \text{ cm}^{-1}$), and stretching modes ($\nu_3/c = 3030 \text{ cm}^{-1}$), respectively (Draine & Li 2001). $\frac{H}{C}$ is the hydrogen to carbon ratio. We adopt the following empirical formula (Li & Draine 2001),

$$\frac{H}{C} = \begin{cases} 0.5 & (N_C < 25) \\ \frac{0.5}{\sqrt{N_C/25}} & (25 < N_C < 100) \\ 0.25 & (N_C > 100) \end{cases}. \quad (81)$$

2.6.2 Dust cooling

The equation of emission of dust grains with radius a is formulated as,

$$4\pi \epsilon(T, a) = 4\pi \left(\pi a^2 \right) \int Q_{\text{abs}}(\lambda) \frac{2h_p c^2}{\lambda^5} \frac{d\lambda}{\exp\left(\frac{h_p c}{\lambda k T}\right) - 1}, \quad (82)$$

where T is the temperature of dust grain and $\epsilon(T, a)$ is the emission power per unit time per unit solid angle. In the case that dust grains do not absorb energy while cooling, since emission energy and changes in internal energy are balanced, the following equation holds,

$$\frac{dE(T, a)}{dT} \frac{dT}{dt} = -4\pi \epsilon(T, a). \quad (83)$$

This equation can not be solved analytically, but we can calculate, but we can get the temperature variation by numerical calculation.

2.6.3 Result of dust temperature distribution

Figure 5 is the result of dust temperature distribution of silicate. The galaxy is the face on ($\mu = 1$) MW-like galaxy model at the age of 13 Gyr. The condition of the galaxy is the same as §2.2.6. The radius of galaxy R_{gal} is 10 kpc and scale height of dust h_d is 150 pc which is the typical scale height of cold dust in the MW (e.g., Binney & Merrifield 1998).

The temperature of small grains is very widely distributed from 1 to 4,000 K. When grain size becomes larger, the temperature range becomes narrower and approaches the equilibrium temperature. The equilibrium temperature is represented by Draine & Lee (1984); Takeuchi et al. (2003) as

$$T_{\text{eq}} \simeq \left(\frac{h_p c}{\pi k} \right) \left[\frac{945u}{960\pi(2\pi A a)h_p c} \right]^{1/6}, \quad (84)$$

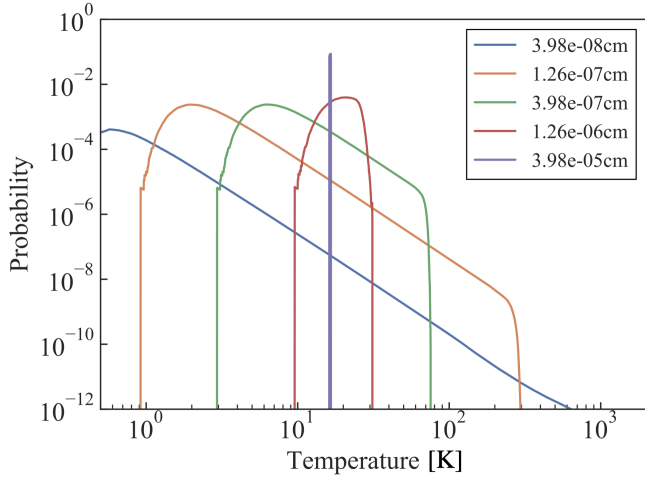


Figure 5. Temperature distribution of the several grain sizes of silicate calculated by Monte Carlo calculation. The blue, orange, green, red, and purple curves indicate 3.98×10^{-8} , 1.26×10^{-7} , 3.98×10^{-7} , 1.26×10^{-6} , and 3.98×10^{-5} cm grains, respectively.

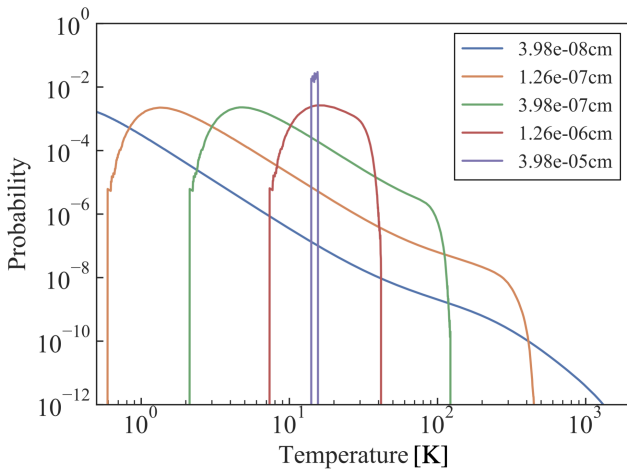


Figure 6. Temperature distribution of the several grain sizes of graphite grain. Calculation parameters and color coordinates are the same as Figure 5.

and

$$u \equiv \int_0^{\infty} u_{\lambda} d\lambda, \quad (85)$$

where h_p is the Planck constant, and we adopt $A_{\text{sil}} = 1.34 \times 10^{-3}$ cm for silicate grains (Drapatz & Michel 1977) and $A_C = 3.20 \times 10^{-3}$ cm for carbonaceous grains (Draine & Lee 1984). When grain size is 3.98×10^{-5} cm, the equilibrium temperature of that grain is about 19 K by Equation (84) and it is equal to the result calculated by the Monte Carlo calculation.

Figure 6 is the temperature distribution of graphite. Graphite grains have broad temperature compared with silicate grains in Figure 5. The difference comes from differences of internal energy between silicate and graphite.

We show the temperature distribution of PAH in Figure 7. Comparing PAH temperature distribution with graphite, PAHs stay in a narrower temperature range because PAHs have an additional term

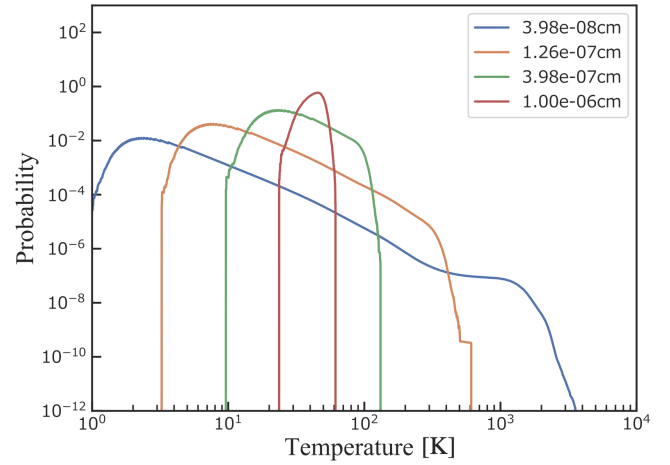


Figure 7. Temperature distribution of the several grain sizes of PAHs. Calculation parameters are the same as Figure 5. The blue, orange, green, and red curves indicate 3.98×10^{-8} , 1.26×10^{-7} , 3.98×10^{-7} , 1.00×10^{-6} cm grains, respectively.

in the equation of internal energy (Equation 80). Almost the same behavior is seen in the result of Draine & Li (2007). From the result of temperature distribution, some dust grains might exceed the sublimation temperature, which is 1500 K or higher (e.g., Baskin & Laor 2018). If we assume that the grain above 1500 K has sublimated and calculated its effect by removing it from the galaxy, the mass of the sublimated grains is only a few percent of the total dust mass. Thus, the effect of the sublimation for the result is negligible, and we do not consider the effect of sublimation temperature in our model for simplicity.

2.7 Dust radiation

The dust radiation depends on the temperature distribution $\frac{dP_i(a)}{dT}$ calculated by the method of the above sections. The monochromatic luminosity of a dust grain of species i (silicate, graphite, neutral PAH, or ionized PAH) is expressed as

$$L_i^{\text{grain}}(a, \lambda) = 4\pi a^2 \pi \int Q_{\text{abs}}^i(\lambda) B_{\lambda}(T) \frac{dP_i(a)}{dT} dT, \quad (86)$$

where B_{λ} is the blackbody radiation and Q_{abs}^i is the absorption coefficient of dust species i . Total luminosity at wavelength λ is represented as,

$$L(\lambda) = \sum_i Q_{\text{abs}}^i(\lambda) \int L_i^{\text{grain}}(a, \lambda) f_i(a) da. \quad (87)$$

$f_i(a)$ is the dust number distribution of dust species i from the dust evolution model.

3 RESULT: MILKY WAY-LIKE GALAXY MODEL SED

In Figure 8, we show the model result with a face-on ($\mu = 1$) MW-like galaxy model (§2.6.3 and §2.2.6) at the age of 13 Gyr (the same setting as §2.6.3). Each curve in Figure 8 represents the corresponding emission species. At the 912 Å wavelength, we see the cutoff of the Lyman break. The UV to IR wavelength region is dominated by stellar emission. Numerous PAH lines are prominent in the mid-IR, and the far-IR range is dominated by the continuum emission from

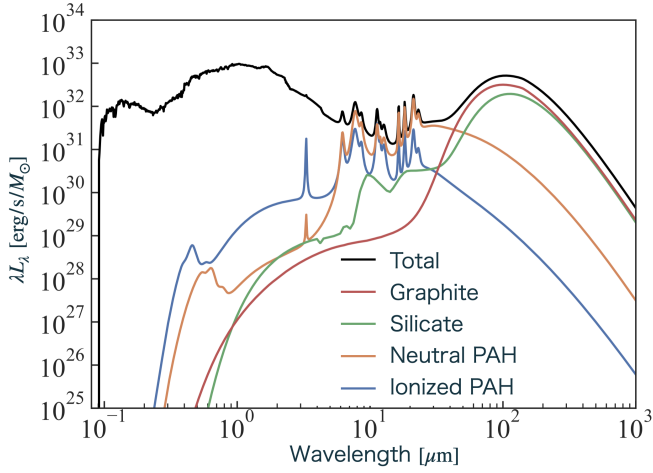


Figure 8. The result of our SED model with MW-like galaxy parameters at an age of 13 Gyr. The black curve represents the overall emission of the galaxy. Other color curves express each dust species (blue: ionized PAH, orange: neutral PAH, green: silicate, red: graphite).

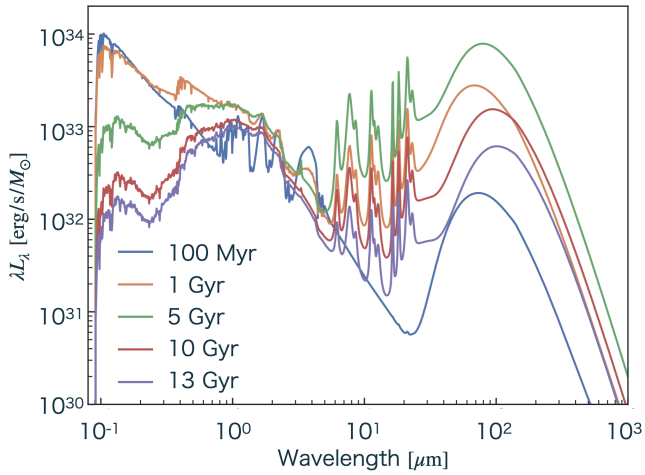


Figure 9. The evolution of the SED of a MW-like galaxy. Parameters are the same as Figure 8. Blue, orange, green, red, and purple curves indicate age of 100 Myr, 1, 5, 10, 13 Gyr, respectively.

large graphite grains. The emission of silicate is weaker than that of graphite in the wavelength range of $200 \mu\text{m}$ or less, and is effective only in the longer wavelength range. The temperature of graphite and silicate fitted by a gray body are 28 K and 26 K, respectively. The difference in emission and temperature between graphite and silicate is caused by the number of grains.

Figure 9 is the time evolution of our galaxy SED model with the MW-like galaxy model parameters. The purple curve represents the SED of a MW-like galaxy at the age of 13 Gyr, as Figure 8. Blue, orange, green, and red curves represent the age of 100 Myr, 1, 5, and 10 Gyr, respectively. Figure 9 shows that the UV region emitted by stars monotonically decreases with the evolution. Since we assume a closed box, the gas mass decreases monotonically as it is consumed by star formation. The SFR is proportional to the gas mass, hence SFR also decreases monotonically, and the UV radiation also decreases. The overview of the time evolution of the SED is as follows.

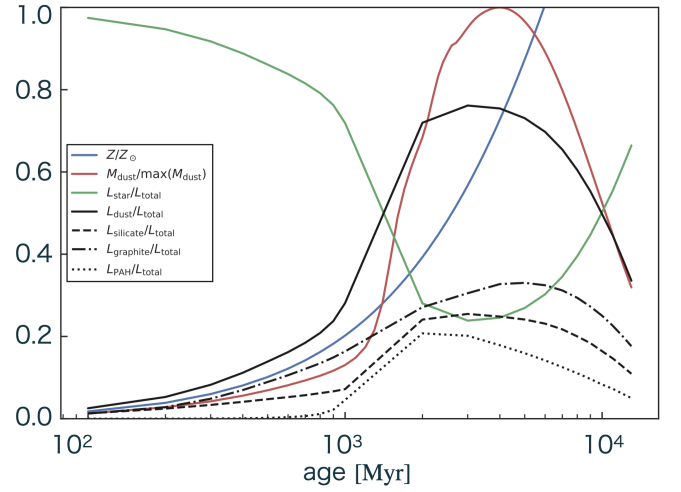


Figure 10. The evolution of metallicity, dust mass, and bolometric luminosity of each component of the galaxy. Parameters are set to be the same as Figure 8. Metallicity, dust mass, and bolometric luminosities are normalized by solar metallicity $Z_{\odot} = 0.02$ (Anders & Grevesse 1989), maximum value of it, and overall bolometric luminosity, respectively. The calculation was performed with the age of the logarithmic scale bin.

- <100 Myr
 - Stellar emission dominates the SED and PAH emission does not exist yet.
- 100 Myr–1 Gyr
 - Stellar emission still dominates the SED, but the dust emission including PAH gradually becomes prominent.
- 1–5 Gyr
 - Dust emission dominates the SED and dust emission becomes strongest at this age.
- 5–13 Gyr
 - The emission both from stars and dust gradually decreases, along with the decline of the star formation rate.

The details of the SED evolution are explained below.

At 100 Myr, since only a very small amount of dust has been produced, stellar radiation is not attenuated, and dust radiation is weak. Particularly, PAHs are not produced in young galaxies, hence the MIR radiation is very faint. For an SED model that supposes a constant size distribution without considering the evolution of the dust size distribution (e.g., Schurer et al. 2009), many PAHs are observed even in such young galaxies, and different conclusions are deduced.

The evolution of metallicity, dust mass and bolometric luminosity for each component are shown in Figure 10. The dust mass is normalized with respect to its maximum value. Dust mass and luminosity are tightly correlated. Here we adopt $Z_{\odot} = 0.02$ (Anders & Grevesse 1989). At 1 Gyr, the dust mass is gradually increasing, and along with this, the IR radiation from dust becomes prominent. Because the PAH mass increases by the evolution in the ISM, their characteristic mid-infrared line emission can be seen.

The dust emission becomes strongest at 3 Gyr if we adopt the star formation timescale $\tau_{\text{SF}} = 3$ Gyr. As predicted, in the MW-like model, when the metallicity exceeds $0.1 Z_{\odot}$, the metal accretion

process becomes effective and the dust mass increases (Asano et al. 2013a). Star formation is active, but the UV continuum from young stars is strongly attenuated due to the increase of dust mass.

After 3 Gyr, the dust mass decreases due to the destruction by SN shocks and astration. Dust radiation also decreases with the age of the galaxy. This is not only due to the reduction of dust mass, but also due to the decline of the UV light from young stars to heat dust grains.

Focusing on the metallicity, it reaches $1.6 Z_{\odot}$ at 13 Gyr, which is larger than the solar metallicity. This is due to the assumption of the closed box model. In the closed box model, there is no inflow of gas and outflow of ISM and the metallicity increases monotonically. However, considering the infall model, the metallicity is reduced because the ISM is diluted by the inflow of gas (Erb et al. 2006).

We should note the difference in the evolution of each species of dust grains in Figure 10. The increase of graphite emission is more gradual than the increase of other components. The metallicity of a galaxy exceeds the critical metallicity in accretion onto the dust surface, leading to the sharp rise of the dust mass and emission (Asano et al. 2013a). Shattering produces small dust grains and makes the surface area of dust larger, and consequently leads to the boost of the accretion efficiency. However, since we regard almost all small carbonaceous grains as PAHs, the mass of graphite grains does not have the discontinuous increase. The bolometric luminosity of dust emission is dominated by graphite in all epochs.

4 DISCUSSION

4.1 Effect of star formation timescale

The effect of star formation (SF) timescale τ_{SF} is shown in Figure 11. In Figure 11, the SEDs are calculated with different SF timescale and age from Figure 8, while geometrical parameters are kept the same. The galaxy age increase from left to right the panels (100 Myr, 1, and 10 Gyr), and SF timescale increase from top to bottom the panels ($\tau_{\text{SF}} = 0.5, 1, 5$ Gyr). Three characteristic trends are observed in Figure 11. First, the UV light emitted by stars and the IR light emitted by graphite and silicate grains at the age of 100 Myr decrease with increasing τ_{SF} . This is because the age of the galaxy is sufficiently small with respect to the SFR, and the larger the time scale of the star formation rate, the fewer stars form. In these young galaxies, PAHs are not produced and the PAHs emission is not observed in the model with any τ_{SF} yet. This indicates that the dust mass in early galaxies is dominated by production from stars instead of accretion processes.

Second, the overall bolometric luminosities tend to be stronger when the age of the galaxy is equal to the SF timescale. In this evolutionary phase, the SFR is still large and a large amount of dust exists in the galaxy.

Lastly, when the age of the galaxy is older than the SF timescale, the galaxy has very weak stellar emission due to consumption of most of the gas in the ISM which is an ingredient of star formation. The dust emission is also very weak in the galaxy because both, decreasing dust mass and UV light which is the source of heating dust grains.

4.2 Effect of geometrical parameters

Figure 12 shows the effect of changing the dust scale height of galaxy h_{d} for our galaxy SED model at an age of 13 Gyr. The SFH is the same as Figure 8. Blue, red, and green curves represent $h_{\text{d}} = 75, 150$ (fiducial), and 300 pc, respectively. Intrinsic stellar radiation does

not depend on h_{d} . Since the optical depth of the galaxy is defined as $\tau = \kappa_{\text{eff}} h_{\text{d}}$, τ increases as h_{d} increases. Then, the absorption by the dust grain becomes stronger, and the observed UV radiation becomes weaker. Since the energy absorbed by the dust grain increases, the radiation in the IR region becomes stronger.

Since our SED model assumes an axisymmetric one-dimensional disk, the galaxy has no structure in the radial direction and does not determine the radius. However, in reality, when the radius of the galaxy changes and the volume changes, the density of the dust clump changes and the optical depth also changes. In our model, the optical depth depends on clump filling fraction (Equation (49)), and we assume that n_{H} is constant. Therefore, if we consider a galaxy with a volume in which n_{H} changes significantly from 1 cm^{-3} , it is necessary to consider it, but it is not implemented in our model and is a future work.

4.3 Effect of the ISM phase fraction

In the current model, we consider three phases in the ISM: WNM, CNM and MC. Figure 13 and 14 are the effects of the ISM phase fraction for dust size distribution. The parameters except the ISM fraction are the same as the MW-like galaxy. The value of the fraction of cold region η is changed while keeping the ratio in the cold region constant to $\eta_{\text{CNM}} : \eta_{\text{MC}} = 3 : 2$ in this section. Solid, dashed, and dot-dashed curves represent fiducial, $\eta = 1$ ($\eta_{\text{WNM}} = 0.0, \eta_{\text{CNM}} = 0.6, \text{ and } \eta_{\text{MC}} = 0.4$), and $\eta = 0$ ($\eta_{\text{WNM}} = 1.0, \eta_{\text{CNM}} = 0.0, \text{ and } \eta_{\text{MC}} = 0.0$) case, respectively.

At 100 Myr galaxy, there is no difference in three cases, since the stellar production dominates dust size distribution and is not affected by the ISM fractions.

At 1 Gyr galaxy, the size distribution of small η cases have small amount of grain in radius of $> 2 \times 10^{-1} \mu\text{m}$ region because shattering is more likely to occur thanks to collisions between larger grains. The bump in $10^{-3} - 10^{-2} \mu\text{m}$ is generated by accretion on the $> 10^{-3}$ size of the grain surface. The bump is not observed in the $\eta = 0$ case, because in this case the accretion process on grains in the cold regions is not included. The $\eta = 1$ result has a larger bump than the fiducial case. This is because shattering is not effective yet, and the larger the fraction of cold regions is, the more effective the metal accretion. On the contrary, large amounts of intermediate size grains ($2 \times 10^{-2} - 2 \times 10^{-1} \mu\text{m}$) in a small η case. This results from the coagulation process in WNM.

At the 13 Gyr galaxy, a small amount of grain is observed in the $\eta = 0$ case. When grain evolution occurs in only WNM, a strong shattering process generates the large amount of small grains. Small dust grains are largely destroyed by SN shock (Nozawa et al. 2006), hence the mass of dust grains effectively decreases. The large bump in $10^{-1} \mu\text{m}$ is caused by the balance between strong shattering and coagulation. At the grain sizes of $< 1 \mu\text{m}$, the size distribution of the $\eta = 1$ case has a smaller amount of dust. This is because the shattering is weak in the $\eta = 1$ case and the metal accretion does not occur as effectively as the fiducial case, because the WNM is not considered in the calculation of the dust evolution. Further, maximum grain radius in the $\eta = 1$ case reaches $> 1 \mu\text{m}$, as weak shattering efficiency in CNM and MC.

The effect of η for total dust mass of the MW-like galaxy model is shown in Figure 14. Very small amount of total dust mass is observed in the $\eta = 0$ case because the case does not consider the mass-increasing process other than the production from the stars. Around 1 Gyr, the $\eta = 1$ case has a larger amount of total dust mass than the fiducial case. This is because shattering is still less effective in this age, and metal accretion dominates the increase of total dust

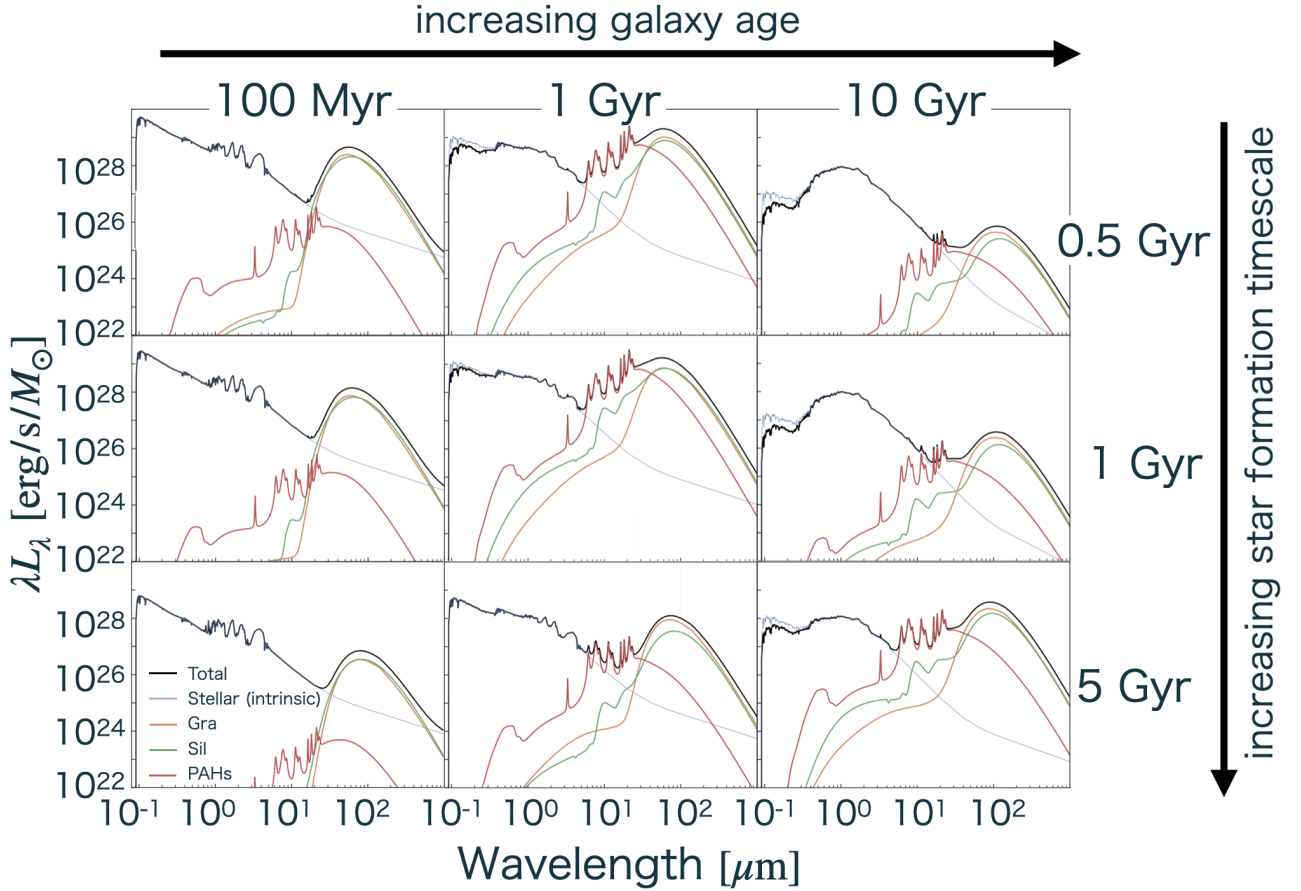


Figure 11. The effect of star formation timescale τ_{SF} for galaxy SED. The geometrical model parameters are the same as Figure 11. The galaxy age is increasing from left to right, SF timescale increases from top to bottom. The age and SF timescale are written on each plot. Black, orange, green, red thick curves represent overall, graphite, silicate, and PAHs luminosity, respectively. Blue thin curve is an intrinsic (unattenuated) stellar emission.

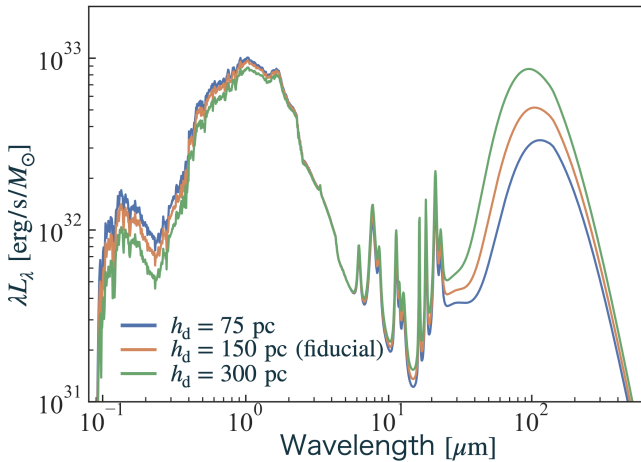


Figure 12. Galaxy SEDs with various dust scale heights h_d at the age of 13 Gyr. The star formation history is the same as Figure 8. Blue, orange, and green curves represent 75, 150 (fiducial), and 300 pc, respectively.

mass. After 1 Gyr, the increase of total dust mass in the $\eta = 1$ case is slower than that in the fiducial case, since the rapid increase cycle is less effective in the $\eta = 1$ case. The total mass at 13 Gyr is determined

by the balance between destruction by SN shocks and the dust growth by metal accretion.

The galaxy SED at 13 Gyr with the cold ISM region fraction $\eta = 0.5$ (fiducial, solid orange), 1 (dashed blue), and 0 (dot-dashed green). In $\eta = 0$ case, the SED has weaker dust attenuation and dust radiation than that of the fiducial case (Figure 14), since dust mass in all radius is smaller than the fiducial case. Though the difference of total dust mass between the fiducial and the $\eta = 1$ case is small, the size distribution of the two cases has a large difference. The $\eta = 1$ case has a lot of large dust grains and a few small dust grains. The attenuation in the $0.1 \mu\text{m}$ wavelength is mainly dominated by the $a < 1 \mu\text{m}$ radius of grain. As the large grain has large heat capacity, the radiation from the large grain is weaker than that from the small grain. Therefore, $\eta = 1$ case has weaker attenuation in the UV region and weaker radiation in the IR region than the fiducial case.

4.4 Effect of the coagulation threshold

Coagulation can occur when the relative velocity of grains v_{coag} is slower than the threshold velocity. However, we do not adopt the threshold of coagulation to reproduce the dust size distribution of the MW (Asano et al. 2013a; Nozawa et al. 2015). If v_{coag} is adapted to the dust model, since the small radius grains have lower relative velocity, the small grains are more likely to coagulate. Conversely, the large radius grains have large relative velocity and the grains cannot

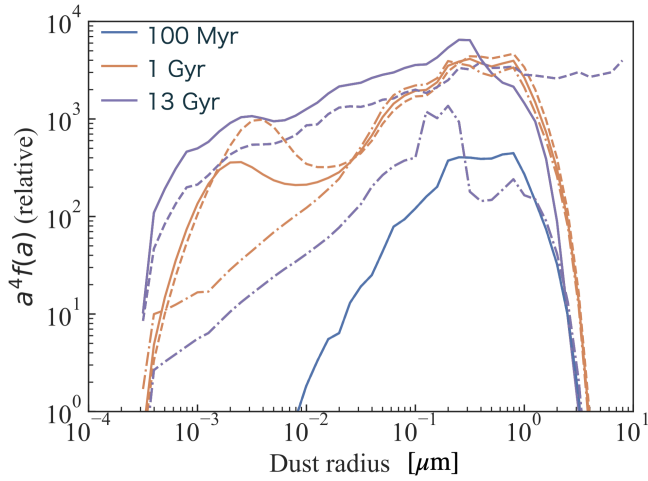


Figure 13. The dust size distribution with cold ISM region fraction $\eta = 0.5$ (fiducial, solid), 1 (dashed), and 0 (dot-dashed). Blue, orange, and purple curves are the age of 100 Myr, 1, and 13 Gyr galaxies, respectively. Note, the 100 Myr galaxy has three overlapping curves.

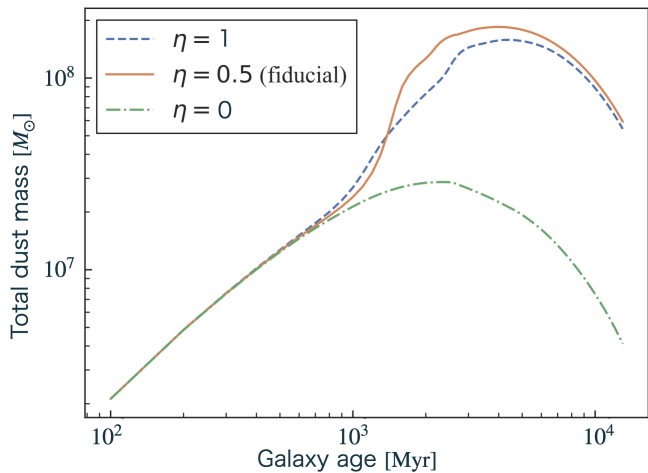


Figure 14. The evolution of total dust mass with $\eta = 0.5$ (fiducial, orange solid), 1 (blue dashed), and 0 (green dot-dashed).

occur the coagulation. [Hirashita & Yan \(2009\)](#) show that the grain radius increases only up to $0.01\text{--}0.1\ \mu\text{m}$, because the radii $a > 0.1\ \mu\text{m}$ grains have the relative velocity larger than v_{coag} . Therefore, a lower coagulation threshold velocity suppresses the effect of coagulation. First, we show the effect of v_{coag} for total dust grain mass in [Figure 16](#). The dashed and solid lines represent the fiducial case (no v_{coag}) and the adopted v_{coag} case (we call it a suppressed coagulation case). Galaxy parameters are the same as [§2.2.6](#) except v_{coag} . We calculate the coagulation velocity threshold in the same formula as [Hirashita & Yan \(2009\)](#). v_{coag} between grain 1 and 2 is represented as

$$v_{\text{coag}} = 21.4 \left[\frac{a_1^3 + a_2^3}{(a_1 + a_2)^3} \right]^{1/2} \frac{\gamma^{5/6}}{E^{1/3} R_{1,2}^{5/6} s^{1/2}}, \quad (88)$$

where suffix 1 and 2 represents the each value of grain 1 and 2, $R_{1,2} \equiv a_1 a_2 / (a_1 + a_2)$ is the reduced radius of the grains, γ is the surface energy per unit area, and E is related to the Poisson

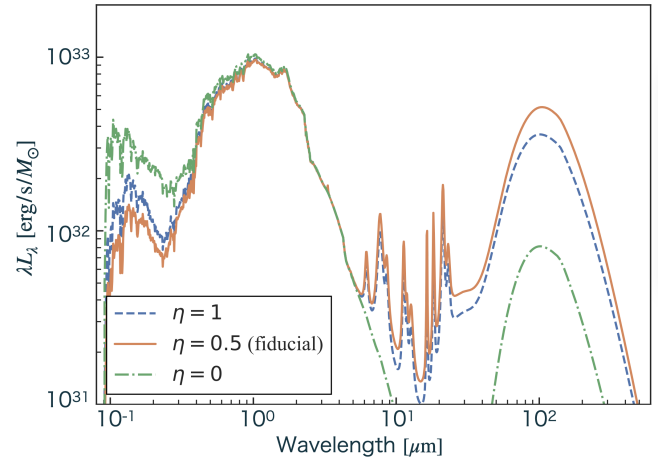


Figure 15. The galaxy SED at 13 Gyr with $\eta = 0.5$ (fiducial, orange solid), 1 (blue dashed), and 0 (green dot-dashed). The parameters are the same as the MW-like galaxy model except η .

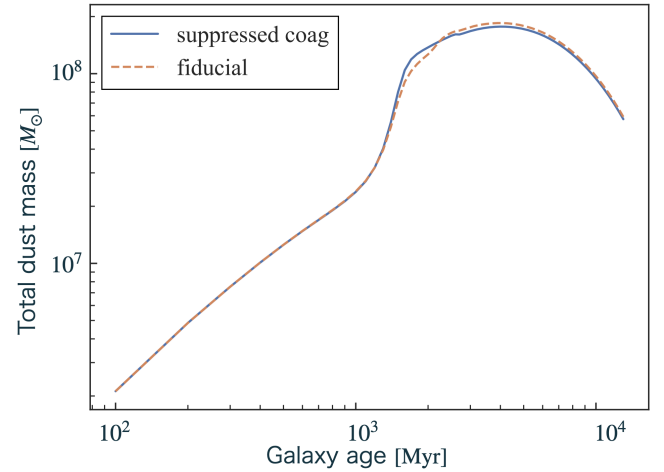


Figure 16. The effect of coagulation threshold velocity for total dust mass. Solid and dashed curves represent suppressed coagulation and fiducial case, respectively. The galaxy properties are the same as the MW-like galaxy model except v_{coag} .

ratios (v_1 and v_2) and the Young modulus (E_1 and E_2) by $1/E \equiv (1 - v_1)^2/E_1 + (1 - v_2)^2/E_2$. The value of γ , v , and E are $25\ \text{erg}/\text{cm}^2$, $0.17\ \text{erg}/\text{cm}^2$ and $5.4 \times 10^{11}\ \text{dyn}/\text{cm}^2$ for silicate, and $12\ \text{erg}/\text{cm}^2$, 0.5 and $3.4 \times 10^{10}\ \text{dyn}/\text{cm}^2$ for graphite from [Chokshi et al. \(1993\)](#). From [Figure 16](#), the effect of v_{coag} for total dust mass is very small. Coagulation itself decrease total surface area of grains and suppress the cross section of the metal accretion. On the other hand, as the grain size increases, shattering is more likely to occur, and smaller radius grain increases. Since these effects are balanced, coagulation only suppresses the increase in total dust mass and has a small effect. Coagulation is difficult to occur in young galaxies (age > 1 Gyr), and becomes effective after the shattering process becomes effective. Therefore, when the coagulation becomes effective, the rapid increase in the total dust grain mass has already finished, and the coagulation does not significantly affect the total mass, but only changes the size distribution of the dust grain.

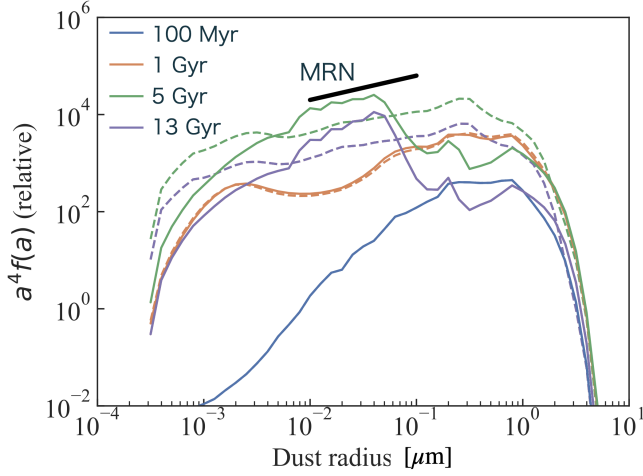


Figure 17. The effect of v_{coag} for dust size distribution. Blue, orange, green, and purple curves represent the dust grain size distribution with the age of 100 Myr, 1 Gyr, 5 Gyr, and 13 Gyr, respectively. Solid and dashed lines represent suppressed coagulation and fiducial case, respectively.

Second, we show the effect of v_{coag} for dust size distribution in Figure 17. In the age of the 100 Myr and 1 Gyr galaxies, since effective dust evolution in the ISM has not started yet, there is no difference in the dust size distribution between the two cases. On the other hand, v_{coag} strongly affects the dust distribution after 1 Gyr galaxy. v_{coag} suppresses the coagulation between larger grains and determines the maximum radius of dust grain. Coagulation shifts the size distribution to larger sizes, thus, in the suppressed coagulation case, the dust size distribution is biased toward the smaller one, and the slope is also different from MRN. Therefore, adopting the low v_{coag} in the MW-like galaxy model leads to the dust size distribution to be different from the MRN distribution, and thus we do not adopt v_{coag} in our model.

4.5 Comparison between closed-box and infall model

The comparison between the result of the closed-box and infall model is shown in Figure 18. We adopt the following equation for the infall rate (Inoue 2011):

$$\frac{dM_{\text{infall}}}{dt} = \frac{M_{\text{infall}}}{\tau_{\text{infall}}} \exp\left(-\frac{t}{\tau_{\text{infall}}}\right), \quad (89)$$

where τ_{infall} is the timescale of infall, and M_{infall} is the total mass that flows into the galaxy by infall as $t \rightarrow \infty$. For the infall model, the initial mass of a galaxy is set to zero, and primordial gas (zero-metallicity) fall onto the galaxy with $M_{\text{infall}} = 10^{11} M_{\odot}$ and $\tau_{\text{infall}} = 6$ Gyr. The time evolution of the SFR and dust mass are plotted in Figure 19. The star formation history is very different between the two models. While the SFR of the closed-box model case monotonically decrease, the SFR of the infall model gradually increase and it reaches to a peak at $t_{\text{gal}} = 5$ Gyr (close to infall timescale $t_{\text{infall}} = 6$ Gyr), after that the SFR decrease gradually. Since the SFR at 13 Gyr of the infall model is higher than that of the closed-box model, the ratio of younger stars is increased in the infall model, and then the luminosity of the UV region becomes stronger. On the other hand, the continuum at near IR wavelengths emitted from old stars becomes slightly weaker due to the smaller amount of old stars. The metallicity is $1.6 Z_{\odot}$ in the closed box model, while it is $0.86 Z_{\odot}$ in the infall model which is closer to the solar metallicity.

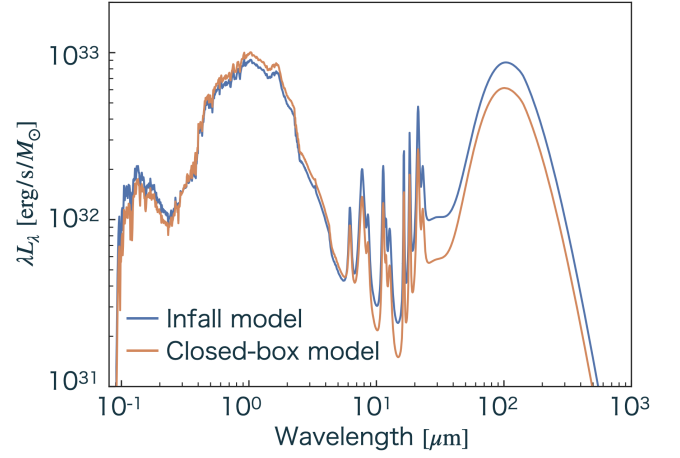


Figure 18. The comparison of MW-like model galaxy SED at age $t_{\text{gal}} = 13$ Gyr with infall and closed-box model. The orange curve represents closed-box model (same as Figure 8), the blue curve represents infall model with infall time scale $\tau_{\text{infall}} = 6$ Gyr.

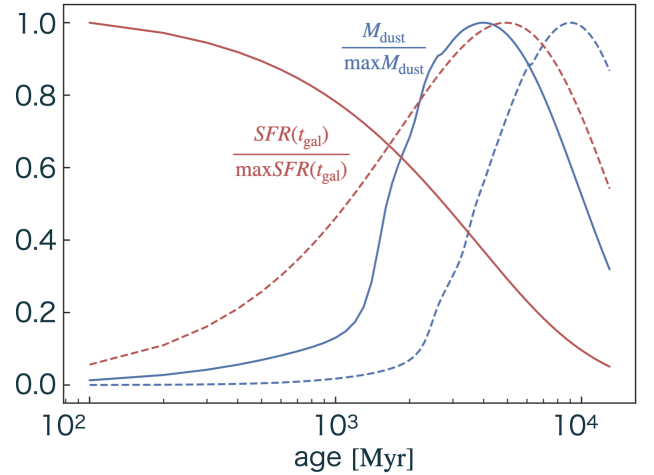


Figure 19. The time evolution of dust mass and SFR of the galaxy with closed-box and infall model (same galaxies as Figure 18). Colors represent the difference of quantities: the ratio of SFR(t_{gal}) and maximum value of it (red), and the ratio of dust mass M_{dust} and maximum value of it (blue). The solid and dashed curves represent closed-box and infall models, respectively.

In the infall model case, the peak of the dust mass comes later because of the different star formation history. It leads to an increase of the IR emission which is emitted by dust grains. In general, the infall model tends to delay the evolution of the galaxy.

4.6 Radio emission

Our model does not include the radio emission. Because, in a normal galaxy, the luminosity of the radio region is only $< 10^{-4}$ of the overall bolometric luminosity of a galaxy (Condon 1992). Above ~ 1 mm, radio emission is swamped in dust emission for normal galaxies. The radio is mainly emitted by synchrotron radiation from relativistic electrons accelerated in supernova remnants and free-free emission by HII region, which is a ionized by the radiation of heavy

and young stars (Klein et al. 1988; Carlstrom & Kronberg 1991). Since both radio sources are associated with SN explosions, their radiation is considered to depend on the SN rate (SNR) (Condon 1992). In particular, many galaxies with strong synchrotron radiation by a jet from active galactic nuclei have been observed (e.g., Carilli et al. 1991; Laing & Bridle 2002), and we will take it into account in our future work.

5 CONCLUSIONS

In this paper, we construct a new galaxy SED model including the dust evolution in galaxies consistent with the chemical evolution (Asano et al. 2013a,b, 2014). The dust model considers several evolutionary processes of the dust production by AGB stars and SNe II, the destruction by SN shocks in the ISM, the grain growth by metal accretion to grain surface, and the two types of grain-grain collision, the shattering and coagulation. The stellar radiation is calculated by PÉGASE.2 (Fioc & Rocca-Volmerange 1999). Based on this, we constructed a radiative transfer model with a one-dimensional plain parallel geometry equipped with the mega-grain approximation for fast computation (Varosi & Dwek 1999; Inoue 2005). For the radiation from dust, we take into account the stochastic heating of dust grains by Monte Carlo simulation. As a fiducial model, we assumed the Schmidt law with star formation time scale $\tau_{\text{SF}} = 3$ Gyr, the Salpeter IMF (Salpeter 1955), and the closed box model. The ISM phase fractions were set as $\eta_{\text{WNM}} = 0.5$, $\eta_{\text{CNM}} = 0.3$, and $\eta_{\text{MC}} = 0.2$, scale height of dust is $h_{\text{d}} = 150$ pc, and the threshold of coagulation velocity is removed. Our model indicates that early galaxies (~ 100 Myr) produce a small amount of dust. The PAHs, which dominate the MIR wavelength region, have not been produced yet, in particular. The SED at the age of 100 Myr is dominated by stellar emission. Then the amount of dust mass and emission explosively increases at the age of about 3 Gyrs. Subsequently, the dust mass and emission from both the stars and dust decreases, along with the decline of the star formation rate. Since this model treats the evolution of dust appropriately, we can apply it to any age of a galaxy as far as the model assumptions are valid.

ACKNOWLEDGEMENTS

First of all, we offer our sincere thanks to the anonymous referee for her/his enormous effort to read through the article and invaluable important comments and suggestions that improved the quality of the paper very much. We are grateful to the colleagues in the Lab for fruitful discussions and comments. We thank H. Kobayashi and A.K. Inoue for helpful comments on the coding of dust evolution model. This work has been supported by JSPS Grants-in-Aid for Scientific Research (17H01110, 19H05076, and 21H01128). This work has also been supported in part by the Sumitomo Foundation Fiscal 2018 Grant for Basic Science Research Projects (180923), and the Collaboration Funding of the Institute of Statistical Mathematics “New Development of the Studies on Galaxy Evolution with a Method of Data Science”.

DATA AVAILABILITY

The data underlying this article will be shared on reasonable request to the corresponding author.

REFERENCES

- Alongi M., Bertelli G., Bressan A., Chiosi C., Fagotto F., Greggio L., Nasi E., 1993, *A&AS*, 97, 851
- Anders E., Grevesse N., 1989, *Geochim. Cosmochim. Acta*, 53, 197
- Arendt R. G., et al., 2010, *ApJ*, 725, 585
- Arons J., Max C. E., 1975, *Astrophys. J.*, 196, L77
- Asano R. S., Takeuchi T. T., Hirashita H., Inoue A. K., 2013a, *Earth, Planets Sp.*, 65, 213
- Asano R. S., Takeuchi T. T., Hirashita H., Nozawa T., 2013b, *MNRAS*, 432, 637
- Asano R. S., Takeuchi T. T., Hirashita H., Nozawa T., 2014, *Mon. Not. R. Astron. Soc.*, 440, 134
- Baskin A., Laor A., 2018, *Mon. Not. R. Astron. Soc.*, 474, 1970
- Bertelli G., Bressan A., Chiosi C., Fagotto F., Nasi E., 1994, *A&AS*, 106, 275
- Bianchi S., Schneider R., 2007, *Mon. Not. R. Astron. Soc.*, 378, 973
- Binney J., Merrifield M., 1998, *Galactic Astronomy*
- Biscaro C., Cherkneff I., 2016, *Astron. Astrophys.*, 589, 1
- Bohren C. F., Huffman D. R., 1983, *Absorption and scattering of light by small particles*. New York: Wiley, <https://ui.adsabs.harvard.edu/abs/1983asls.book.....B>
- Borkowski K. J., et al., 2006, *ApJ*, 642, L141
- Bressan A., Fagotto F., Bertelli G., Chiosi C., 1993, *A&AS*, 100, 647
- Burgarella D., Nanni A., Hirashita H., Theulé P., Inoue A. K., Takeuchi T. T., 2020, *Astron. Astrophys.*, 637, A32
- Calura F., Pipino A., Matteucci F., 2008, *A&A*, 479, 669
- Carilli C. L., Perley R. A., Dreher J. W., Leahy J. P., 1991, *ApJ*, 383, 554
- Carlstrom J. E., Kronberg P. P., 1991, *ApJ*, 366, 422
- Cazaux S. M., Caselli P., Walmsley M., Tielens A. G., 2005, *Proc. Int. Astron. Union*, 1, 325
- Ceccarelli C., Viti S., Balucani N., Taquet V., 2018, *Mon. Not. R. Astron. Soc.*, 476, 1371
- Chokshi A., Tielens A. G. G. M., Hollenbach D., 1993, *ApJ*, 407, 806
- Condon J. J., 1992, *ARA&A*, 30, 575
- Conroy C., 2013, *ARA&A*, 51, 393
- De Looze I., et al., 2020, *Mon. Not. R. Astron. Soc.*, 496, 3668
- De Vis P., et al., 2017, *Mon. Not. R. Astron. Soc.*, 471, 1743
- De Vis P., et al., 2019, *Astron. Astrophys.*, 623, A5
- Draine B. T., 2009, *Space Sci. Rev.*, 143, 333
- Draine B. T., Anderson N., 1985, *ApJ*, 292, 494
- Draine B. T., Lee H. M., 1984, *ApJ*, 285, 89
- Draine B. T., Li A., 2001, *ApJ*, 551, 807
- Draine B. T., Li A., 2007, *ApJ*, 657, 810
- Drapatz S., Michel K., 1977, *A&A*, 56, 353
- Dwek E., 1998, *ApJ*, 501, 643
- Dwek E., Scalo J. M., 1980, *ApJ*, 239, 193
- Dwek E., Galliano F., Jones A. P., 2007, *ApJ*, 662, 927
- Erb D. K., Shapley A. E., Pettini M., Steidel C. C., Reddy N. A., Adelberger K. L., 2006, *Astrophys. J.*, 644, 813
- Evans A., 1994, *The dusty universe*. Wiley, Chichester, <https://ui.adsabs.harvard.edu/abs/1994duun.book.....E>
- Fagotto F., Bressan A., Bertelli G., Chiosi C., 1994a, *A&AS*, 104, 365
- Fagotto F., Bressan A., Bertelli G., Chiosi C., 1994b, *A&AS*, 105, 29
- Fagotto F., Bressan A., Bertelli G., Chiosi C., 1994c, *A&AS*, 105, 39
- Ferrara A., Viti S., Ceccarelli C., 2016, *Mon. Not. R. Astron. Soc. Lett.*, 463, L112
- Field G. B., Goldsmith D. W., Habing H. J., 1969, *ApJ*, 155, L149
- Fioc M., Rocca-Volmerange B., 1999, arXiv e-prints
- Fioc M., Rocca-Volmerange B., 2019, *A&A*, 623, A143
- Gall C., Andersen A. C., Hjorth J., 2011a, *Astron. Astrophys.*, 528, A13
- Gall C., Andersen A. C., Hjorth J., 2011b, *Astron. Astrophys.*, 528, A14
- Gall C., et al., 2014, *Nature*, 511, 326
- Ginolfi M., Graziani L., Schneider R., Marassi S., Valiante R., Dell’Aglia F., Ventura P., Hunt L. K., 2018, *Mon. Not. R. Astron. Soc.*, 473, 4538
- Girardi L., Bressan A., Chiosi C., Bertelli G., Nasi E., 1996, *A&AS*, 117, 113
- Heger A., Fryer C. L., Woosley S. E., Langer N., Hartmann D. H., 2003, *ApJ*, 591, 288
- Hellyer B., 1970, *Obs.*, 90, 55

- Heney L. C., Greenstein J. L., 1941, *Nature*, 147, 613
- Hiraki A., Hirak H., 2008, *Rev. Mex. Física*, 54, 44
- Hirashita H., 2012, *MNRAS*, 422, 1263
- Hirashita H., Aoyama S., 2019, *MNRAS*, 482, 2555
- Hirashita H., Ferrara A., 2002, *Mon. Not. R. Astron. Soc.*, 337, 921
- Hirashita H., Kobayashi H., 2013, *Earth, Planets Sp.*, 65, 1083
- Hirashita H., Kuo T. M., 2011, *MNRAS*, 416, 1340
- Hirashita H., Yan H., 2009, *MNRAS*, 394, 1061
- Hirashita H., Nozawa T., Kozasa T., Ishii T. T., Takeuchi T. T., 2005, *Mon. Not. R. Astron. Soc.*, 357, 1077
- Hobson M. P., Padman R., 1993, *MNRAS*, 264, 161
- Hollenbach D., McKee C. F., 1979, *ApJS*, 41, 555
- Horn K., Perets H. B., Biham O., 2007, arXiv e-prints
- Inoue A. K., 2003, *Publ. Astron. Soc. Japan*, 55, 901
- Inoue A. K., 2005, *Mon. Not. R. Astron. Soc.*, 359, 171
- Inoue A. K., 2011, *Earth, Planets Sp.*, 63, 1027
- Jones A. P., Nuth J. A., 2011, *A&A*, 530, 1
- Jones A. P., Tielens A. G. G. M., Hollenbach D. J., McKee C. F., 1994, *ApJ*, 433, 797
- Jones A. P., Tielens A. G. G. M., Hollenbach D. J., 1996, *ApJ*, 469, 740
- Kalvans J., 2017, *Proc. Int. Astron. Union*, 13, 374
- Klein U., Wielebinski R., Morsi H. W., 1988, *A&A*, 190, 41
- Kobayashi C., Umeda H., Nomoto K., Tominaga N., Ohkubo T., 2006, *ApJ*, 653, 1145
- Koyama H., Inutsuka S., 2002, in 8th Asian-Pacific Reg. Meet. Vol. II. pp 159–160
- Kozasa T., Nozawa T., Tominaga N., Umeda H., Maeda K., Nomoto K., 2009, in *Cosm. Dust - Near Far*. p. 43
- Kuo T. M., Hirashita H., 2012, *Mon. Not. R. Astron. Soc. Lett.*, 424, 34
- Laing R. A., Bridle A. H., 2002, *MNRAS*, 336, 1161
- Laor A., Draine B. T., 1993, *ApJ*, 402, 441
- Laporte N., et al., 2017, *ApJ*, 837, L21
- Lazarian A., Yan H., 2002, *Astrophys. J.*, 566, L105
- Lejeune T., Cuisinier F., Buser R., 1997, *A&AS*, 125, 229
- Lejeune T., Cuisinier F., Buser R., 1998, *Astron. Astrophys. Suppl. Ser.*, 130, 65
- Lesniewska A., Michałowski M. J., 2019, *Astron. Astrophys.*, 624, 4
- Li A., Draine B. T., 2001, *Astrophys. J.*, 554, 778
- Lisenfeld U., Ferrara A., 1998, *ApJ*, 496, 145
- Liu H.-M., Hirashita H., 2019, *Mon. Not. R. Astron. Soc.*, 490, 540
- Maiolino R., Schneider R., Oliva E., Bianchi S., Ferrara A., Mannucci F., Pedani M., Roca Sogorb M., 2004, *Nature*, 431, 533
- Mancini M., Schneider R., Graziani L., Valiante R., Dayal P., Maio U., Ciardi B., Hunt L. K., 2015, *Mon. Not. R. Astron. Soc.*, 451, L70
- Marchenko S. V., 2006, in *Stellar Evol. Low Met. Mass Loss, Explos. Cosmol.* p. 299, <https://ui.adsabs.harvard.edu/abs/2006ASPC...353..299M>
- Mathis J. S., Rumpl W., Nordsieck K. H., 1977, *ApJ*, 217, 425
- Matsuura M., et al., 2019, *Mon. Not. R. Astron. Soc.*, 482, 1715
- McKee C. F., 1989, *ApJ*, 345, 782
- McKee C. F., Ostriker J. P., 1977, *ApJ*, 218, 148
- McKee C. F., Ostriker E. C., 2007, *Annu. Rev. Astron. Astrophys.*, 45, 565
- Michałowski M. J., 2015, *Astron. Astrophys.*, 577, 1
- Michałowski M., Watson D., Hjorth J., 2010, *ApJ*, 712, 942
- Morgan H. L., Edmunds M. G., 2003, *MNRAS*, 343, 427
- Nanni A., Burgarella D., Theulé P., Côté B., Hirashita H., 2020, *Astron. Astrophys.*, 641, A168
- Neufeld D. A., 1991, *ApJ*, 370, L85
- Nozawa T., Kozasa T., Umeda H., Maeda K., Nomoto K., 2003, *Astrophys. J.*, 598, 785
- Nozawa T., Kozasa T., Habe A., 2006, *Astrophys. J.*, 648, 435
- Nozawa T., Kozasa T., Habe A., Dwek E., Umeda H., Tominaga N., Maeda K., Nomoto K., 2007, *Astrophys. J.*, 666, 955
- Nozawa T., Asano R. S., Hirashita H., Takeuchi T. T., 2015, *Mon. Not. R. Astron. Soc. Lett.*, 447, L16
- Ormel C. W., Paszun D., Dominik C., Tielens A. G. G. M., 2009, *Astron. Astrophys.*, 502, 845
- Ossenkopf V., 1993, *Astron. Astrophys.*, 280, 617
- Pipino A., Fan X. L., Matteucci F., Calura F., Silva L., Granato G., Maiolino R., 2011, *A&A*, 525, A61
- Raiteri C. M., Villata M., Navarro J. F., 1996, *A&A*, 315, 105
- Rouillé G., Jäger C., Henning T., 2020, *Astrophys. J.*, 892, 96
- Salpeter E. E., 1955, *ApJ*, 121, 161
- Schmidt M., 1959, *ApJ*, 129, 243
- Schneider R., Hunt L., Valiante R., 2016, *Mon. Not. R. Astron. Soc.*, 457, 1842
- Schurer A., Calura F., Silva L., Pipino A., Granato G. L., Matteucci F., Maiolino R., 2009, *MNRAS*, 394, 2001
- Slavin J. D., Dwek E., Mac Low M.-M., Hill A. S., 2020, *Astrophys. J.*, 902, 135
- Takeuchi T. T., Hirashita H., Ishii T. T., Hunt L. K., Ferrara A., 2003, *Mon. Not. R. Astron. Soc.*, 343, 839
- Takeuchi T. T., Ishii T. T., Nozawa T., Kozasa T., Hirashita H., 2005, *MNRAS*, 362, 592
- Tamura Y., et al., 2019, *ApJ*, 874, 27
- Todini P., Ferrara A., 2001, *MNRAS*, 325, 726
- Valiante R., Schneider R., Bianchi S., Andersen A. C., 2009, *MNRAS*, 397, 1661
- Valiante R., Schneider R., Salvadori S., Bianchi S., 2011, *MNRAS*, 416, 1916
- Varosi F., Dwek E., 1999, *ApJ*, 523, 265
- Ventura P., et al., 2012, *MNRAS*, 2357, 2345
- Ventura P., Criscienzo M. D., Carini R., Antona F. D., 2013, *MNRAS*, 3653, 3642
- Watson D., Christensen L., Knudsen K. K., Richard J., Gallazzi A., Michałowski M., 2015, *Nature*, 519, 327
- Winters J. M., Fleischer A. J., Le Bertre T., Sedlmayr E., 1997, *A&A*, 326, 305
- Wolfire M. G., McKee C. F., Hollenbach D., Tielens A. G. G. M., 2003, *Astrophys. J.*, 587, 278
- Woolsey S. E., Weaver T. A., 1995, *Astrophys. J. Suppl. Ser.*, 101, 181
- Yamasawa D., Habe A., Kozasa T., Nozawa T., Hirashita H., Umeda H., Nomoto K., 2011, *ApJ*, 735
- Yan H., Lazarian A., Draine B. T., 2004, *Astrophys. J.*, 616, 895
- Yasuda Y., Kozasa T., 2012, *ApJ*, 745, 159
- Zhukovska S., 2014, *Astron. Astrophys.*, 562, 1
- Zhukovska S., Gail H. P., Tieloff M., 2008, *A&A*, 479, 453
- da Cunha E., Eminian C., Charlot S., Blaizot J., 2010, *Mon. Not. R. Astron. Soc.*, 403, 1894

This paper has been typeset from a $\text{\TeX}/\text{\LaTeX}$ file prepared by the author.